

Detection of in-plane orbital manoeuvres from a catalogue of geostationary objects

Phuong Linh Ngo

Space Engineering, master's level (120 credits)
2020

Luleå University of Technology
Department of Computer Science, Electrical and Space Engineering

Summary

In the frame of this study, we developed a method in order to detect historical in- plane manoeuvres of satellites on a geostationary orbit. This method is specified for the GEO region because it takes into account the natural perturbations that disturb the orbital state of a satellite. For this reason, the operator has to regularly perform manoeuvres in order to compensate those perturbing forces and maintain the satellite within an orbit configuration that is restricted by the mission requirements. In order to be able to detect manoeuvre, the manoeuvre techniques must be understood. Alternatively, since a manoeuvre changes the orbital state of the spacecraft, the manoeuvre can be detected when the observed data is compared with a reference evolution. In contrast to the observed data, that is affected by the manoeuvre thrust, the reference model shall represent the evolution, the satellite would have followed if the manoeuvre had not been performed. The reference model is represented by the dynamical model STELA that was implemented by the French Space Agency CNES. The observed data is provided by an American space object catalogue that offers a comprehensive and publicly accessible database of objects tracked by the Space Surveillance Network. The TLE database contain the orbital state of each tracked object in the form of mean SGP4 elements in the TEME reference frame. Since the reference model is given by STELA and not by SGP4, the orbital elements need to be converted into mean STELA elements and the frame must be transformed from TEME to the integration frame of STELA. Not all six orbital parameters are interesting to study in terms of in- plane manoeuvres. For example, the evolution of the longitude and of the eccentricity vector is immediately affected by a manoeuvre that changes the shape or the size of an orbit. Consequently, from the equation of motion we derive the change of the orbital parameters affected by a manoeuvre and analyse the historical evolution of only three parameters (longitude and both components of the eccentricity vector). Within the longitude analysis, the manoeuvre epoch is estimated by focusing on the manoeuvre strategy. The spacecraft performs a manoeuvre as soon as the longitude motions threatens to violate the operational deadband. The longitudinal motion is perturbed by the non- spherical Earth gravity field but the spacecraft compensates this perturbation through longitudinal manoeuvres. Consequently, the observed data points follow a parabolic evolution. Two polynomial curves of second degree are laid over the observation: the first curve is derived through a physical approach and the second curve is obtained through a Least square fitting method. In theory, both curves are aligned and the intersection of the fitted parabolas reveals a first estimation of the manoeuvre epoch. In practice, we will analyse the intersection of the LS fitted parabolas. The dispersion between the LS fitted parabolas and the parabola derived from the physical method, represents the quality of the observation depending on the TLE generation process. If the quality of the TLE is less reliable the estimated manoeuvre epoch is less accurate, too, and might deviate from the true epoch by several days. The detected manoeuvre epoch must be companioned by a confidential parameters that denotes the time range around the estimated epoch in which the manoeuvre is expected. The manoeuvre interval is then forwarded to the eccentricity analysis where the manoeuvre epoch is estimated more precisely by studying the divergence between the observed eccentricity behaviour and expected evolution propagated with STELA. The performance of the dynamical reference model strongly depends on the modelling of the perturbation forces. Since the solar radiation pressure, induced by the satellite's effective surface-to-mass ratio, is the most dominant effect that disturbs the eccentricity vector evolution, the propagation relies on an accurate estimation of the S/M. This value is derived by the use of the Levenberg Marquardt optimizer that finds the best S/M estimation by solving the underlying LS problem. As soon as the observed eccentricity vector deviates significantly from the expected evolution given by STELA, the manoeuvre epoch and the velocity increment ΔV of the manoeuvre can be recovered, too.

Keywords: manoeuvre detection, geostationary orbit, perturbations, filters, Two- line elements, station keeping

Contents

1	Introduction	5
2	Objectives	7
3	Theory	8
3.1	Frames	8
3.2	Orbital elements	8
3.2.1	Mean and osculating elements	9
3.3	STELA	11
3.4	Orbital manoeuvres	12
3.4.1	Manoeuvre requirements	12
3.4.2	Station keeping routine	12
3.4.3	Types of manoeuvres	13
3.5	Effects of perturbations on spacecrafts	17
3.5.1	Non-spheric Earth potential	17
3.5.2	Solar Radiation Pressure	19
4	Data pre-processing	20
5	Estimation of the area to mass ratio	21
5.1	Implementation	23
5.2	Tests and verification	24
6	Manoeuvre detection method	26
6.1	Classification of GEO objects	26
6.2	Overview of existing detection methods	27
6.3	Principle of our method	28
6.3.1	Longitude analysis	29
6.3.2	Eccentricity analysis	39
7	Results	43
7.1	Tests	43
7.1.1	Longitude analysis	44
7.1.2	Eccentricity analysis	44
7.2	Discussion	45
7.2.1	Longitude analysis	45
7.2.2	Eccentricity analysis	47
8	Conclusion	51
A	Frames definition	54
B	Radial manoeuvre	55
C	Solar and Lunar attraction	55
D	Longitude acceleration	56

Acknowledgement

I would like to take this opportunity to thank those people who have accompanied me throughout this journey. First of all, thank you to all the supporting people I met at CNES, especially to Vincent Morand and Jean-Francois Goester who were always there to answer my questions during this internship and to Laetitia Azzouzi who helped me with all the administrative issues. Secondly, thanks to you, Peter von Ballmoos, for standing by the side of your students in challenging times and taking the time for weekly meetings with us. Also, thanks for giving me your office for a week when I could not yet return to CNES and the internet broke down at my place. Furthermore, I want to thank my family for always supporting and encouraging me. Cảm ơn, con thương mẹ ba lắm! Also, thanks to my colleagues with whom I could spend a great time at CNES and at office 208. You taught me so many (useful) sentences in French which I will never forget and only use in the appropriate situations. Thanks to Matthias who cooks and does the household for me in very stressful times, even though he is also busy with his own internship and his "start up". Danke für deine liebevolle Fürsorge und dafür, dass du mich auch daran erinnerst zu leben (und nicht nur zu arbeiten).

And my final and biggest thanks goes to my mentor and supervisor Carlos Yanez. I have a huge respect for you and I am very thankful for the possibility of this internship you gave me. Thanks for always being there for me, for always answering my daily mails even in your holidays and when your child was born. Thanks for teaching me so many things in this internship but also for all your advises for example regarding my career.
¡Muchas gracias!

List of Acronyms

BCRF	Barycentric Celestial Reference Frame
cal	Calendar date
CEO	Celestial Ephemeris Origin
CEP	Celestial Ephemeris Pole
CIO	Celestial Intermediate Origin
CIP	Celestial Intermediate Pole
CIRF	Celestial Intermediate Reference Frame
cjd	CNES Julian day
CNES	Centre national d'études spatiales
EME2000	Earth mean equator and equinox at epoch J2000
EOL	End of life
EUMETSAT	European Organisation for the Exploitation of Meteorological Satellites
EW	East - West
FN	False negative
FP	False positive
GB	Great Britain
GCRF	Geocentric Celestial Reference Frame
GEO	Geostationary Orbit
IADC	Inter Agency Debris Coordination Committee
IAU	International Astronomical Union
ICRF	International Celestial Reference Frame
LEO	Low Earth Orbit
LEOP	Launch Early Orbit Phase
LS	Least square
NS	North - South
OPERA	Outil de PrEvision des dates des Rentrées Atmosphériques non contrôlées
P	Positive
S/C	Spacecraft
S/M	Surface to mass ratio
SGP	Simplified General Perturbation model
SK	Station keeping
SRP	Solar radiation pressure
STELA	Semi- analytic Tool for End of Life Analysis
TEME	True Equator Mean Equinox
TLE	Two line element
USA	Unsited States of America
VLBI	Very Long Baseline Interferometry

1 Introduction

On the 30th May 2020 SpaceX successfully launched *Crew Dragon* that shuttled two astronauts to the International Space Station. This event was celebrated not only in the United States, because the nation has launched the crew from American ground, but also globally because it has been a private company that has operated this event. Newspapers report about a so- called "New era"[1] within the space sector that comes with private collaborations. Space activity has grown since 1957, the year in which the human kind has overcome Earth gravity with the first artificial satellite Sputnik. However, the graph below shows that launch traffic is no longer dominated by civil or defence payloads but rather by commercial spacecrafts that lead to crowded orbits around Earth.

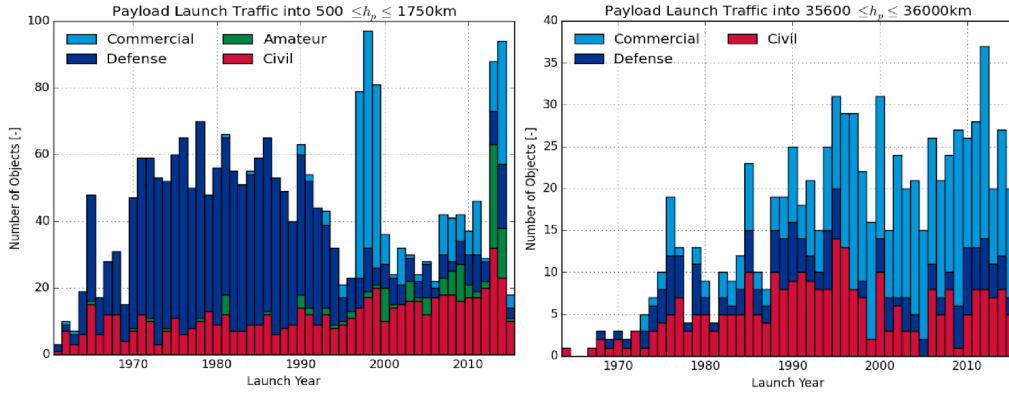


Figure 1: Launch traffic in LEO (left) and in GEO (right) [2]

The larger the population in Earth's orbits the higher the risk of fragmentation and collisions especially between non- operational satellites which have reached their end of mission. In 1978, NASA scientist Donald Kessler and his colleague Burton Cour-Palais warned about in-orbit collisions being the primary source of debris compared to collisions with natural meteoroids. This phenomena known as Kessler syndrome enhances the fragmentation density and further leads to a chain reaction of collisions.[3] The scenario clearly shows the need to control the number of objects in space to maintain an accessible environment also for future explorations and missions. For this reason, the Inter-Agency Space Debris Coordination Committee (IADC) has defined the so- called Protected regions A and B whose "future safe and sustainable use"[4] must be assured at all times.

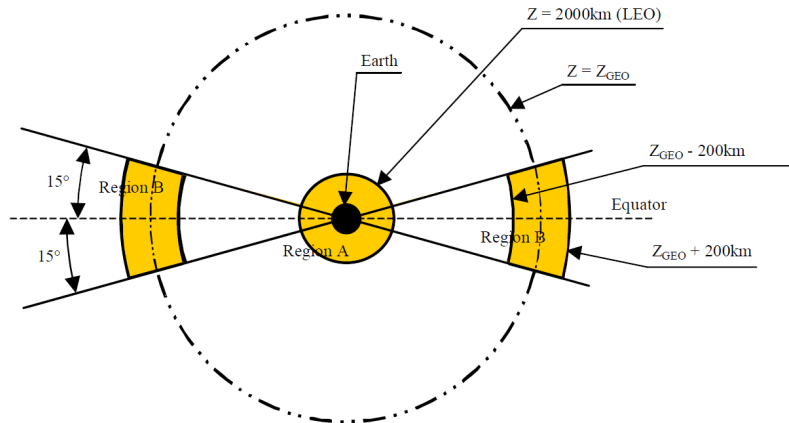


Figure 2: Protected regions [4]

The French Space Operational Act further specifies the operational regulations on a national level. The French Space Agency CNES sees the need of Space surveillance with the objectives to monitor and track space objects close to Earth and analyse their orbital and physical characteristics. Therefore, CNES has developed the Java- based software OPERA whose main task is the prediction of the lifetime of an entire catalogue of objects. In order to predict the lifetime of a spacecraft or specifically, the re-entry of LEO S/Cs into the atmosphere, it is necessary to know when it has reached its end of mission and performed its last manoeuvre. In general, one can consider a satellite as operational if it is still performing station keeping manoeuvres.

This study will focus on the detection of orbital in-plane manoeuvres specifically for GEO objects. OPERA already provides the algorithm to detect manoeuvres in Low Earth orbits by analysing the evolution of the semi- major axis and the inclination vector. In terms of GEO objects, the manoeuvres can not be easily detected with the same method because they encounter different magnitudes of perturbations. Before the start of this project, OPERA has only been capable of classifying GEO objects into six categories: objects which are liberating between the two longitudinal stability points, objects which are at one stable point, object on a drifting orbit, objects which are still operational and objects which have performed their last manoeuvre within the analysed time interval. The main goal of this study is to improve the tool by extending the detection methods also to GEO. Hence, section 2 outlines the milestones of this projects and define the objectives and section 3 explains the theoretical background by giving an introduction into the input parameters, the Two-line elements (TLE), which represents a data format encoding the state of a satellite. The next section shows the requirements of typical manoeuvres for station keeping. Subsection 3.5 focuses on the effects of perturbations in GEO acting on the space objects where we are going to see that the solar radiation pressure (SRP) will significantly perturb the eccentricity vector of a spacecraft proportional to its surface to mass ratio (S/M). Therefore, it is necessary to dedicate section 5 to the estimation of S/M before continuing with the manoeuvre detection methods in section 6. There, we summarize the state of art of the classification algorithm in OPERA for GEO objects and give an overview of the generally existing detection methods. The centre of this project, however, will be the implementation of our detection method and the presentation of the results in section 7.

2 Objectives

The detection of spacecraft manoeuvres requires to analyse the evolution of its state. The spacecraft's state is described by so-called orbital elements. In general, one differentiates between *osculating* and *mean* elements. In the scope of this work, we need to understand the definition of both types before further processing them. In addition, it should be noted that the definition of mean elements is not evident and demands careful treatment when different kinds of propagation models are compared with each other. As indicated previously, data from a TLE catalogue are taken as input that are given as mean elements suitable for the perturbation model SGP4. However, we will see that the SGP4 model is not suitable for the analysis of orbital manoeuvres, instead, we are going to use the dynamic model STELA that comes with a different definition for mean elements. Therefore, it is necessary to differentiate between the types of representation and the conversion from one definition into the other. These orbital elements will be used as inputs of the dynamical model to predict the further behaviour of the spacecraft's state. In a real system, the elements' evolution is complex because it is not only affected by operational manoeuvres but also by (non-) natural perturbations. In fact, the operators have to counteract these disturbing accelerations by performing manoeuvres and the strategy hereby depends on the magnitudes of the perturbations. Consequently, the study will dedicate special attention to the forms of perturbing forces in order to understand the dynamics of GEO objects. The magnitude of these disturbances' effects will not only depend on the orbital regime but also on the physical characteristics of the spacecraft. These parameters are difficult to retrieve because TLEs do not contain (accurate) information about them. Hence, it is necessary to make assumptions on these properties and estimate their value. Among them, the S/M plays a major role since the influence of the solar radiation pressure, which is more dominant in GEO, is proportional to the S/M. In addition, it is necessary to study the different forms of manoeuvres in GEO. Understanding the strategy behind the manoeuvres is essential in order to develop a suitable algorithm to detect them. Numerous methods for manoeuvre detection already exist and their benefits and drawbacks must be critically evaluated to adapt them to our problem. The novel implementation will then take TLE data as input parameters and perform the manoeuvre detection suited for the GEO regime. The performance will then be tested by running the program over historical test objects where the manoeuvre epochs are known in advance.

In summary, the objectives of this study are as follows:

- The dynamical model shall be analysed and understood.
- The dynamics of GEO objects and the forms of perturbations shall be understood.
- The S/M shall be accurately estimated for precise manoeuvre detection.
- The typical in-plane manoeuvres for station keeping shall be understood.
- The existing detection methods shall be analysed in order to adapt them to the present problem.
- A suitable algorithm shall be proposed that is capable of detecting in-plane manoeuvres in GEO.

3 Theory

3.1 Frames

Before being able to specify the orbit of a S/C, it is important to specify the frame in which the state is given. Usually, the frame is defined as a rectangular coordinate system which is based on three unit vectors representing the direction of the axis. All vectors given in this frame are then a linear combination of the three unit vectors. Furthermore, a frame is specified by its origin which can be either defined as the centre of an object or of the entire system, known as the barycentre. Hence, Earth-based system represent a special case since the origin is at the centre of the Earth. In the scope of this study, we will only come across these geocentric frames because our objects of interest are rotating around Earth. Appendix A shows a table with the definition of the main important coordinate frames.[5]

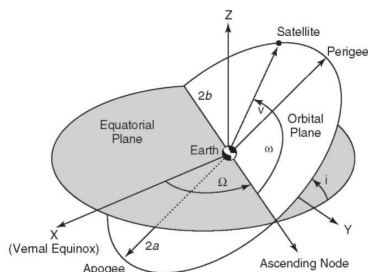
3.2 Orbital elements

Only a few satellite owners have published their history of operation events and for most objects the only source of knowledge about their manoeuvres is through the publicly available Two-line elements sets. These can be downloaded on space-track.org and we will use these TLEs as input data for our algorithm. TLEs are a compact way of representing the S/C's state by means of two lines. TLEs give information on the status of the S/C referring to a specific epoch by means of mean orbital elements. In order to understand the term *mean orbital elements*, it is necessary to recall how the state of a S/C can be generally described.

Line 1	Satellite Number	Line 2	International Designator	Yr	Day of Year (plus fraction)	Epoch	Mean motion derivative (rev/day ²)	Mean motion second derivative (rev/day ³)	Buter (SR)	Elem num
1	1 4 6 0 8	12	8 4 0 1 7 A	9 3	3 5 2	1 3 5 0 2 9 3 4	-0 0 0 0 7 8 8 9	0 0 0 0 0 -0	1 0 5 2 9 -3 0	3 4 2
2	1 4 6 0 8	13	1 1 -6 1 9 0	1 3	-3 3 4 0	0 0 0 5 7 7 0	1 0 2 -9 6 8 0	2 2 7 -5 9 3 0	1 5 -5 9 1 1 4 0 7 0 4 4 7 8 6 9	
			Inclination (deg)	Right Ascension of the Node (deg)	Eccentricity	Arg of Perigee (deg)	Mean Anomaly (deg)	Mean Motion (rev/day)	Epoch	

Figure 3: Structure of a TLE on the example of the Soviet space station MIR [6]

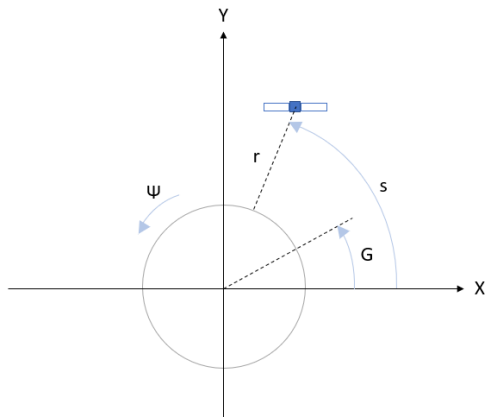
Six quantities are needed in order to represent the dynamical state of any point object in space. An example is the representation through the position and velocity vector. Alternatively, the state can be derived from a set of scalar magnitude and angular quantities of the orbit known as orbital elements.[5] In Figure 4, the orbital elements describe a Keplerian orbit, hence, they are called *Keplerian elements*. However, by focusing on a specific orbit region, we can make use of the orbit's characteristics and find a more explicit way of representing orbital elements.



- Semi-major axis a
- Eccentricity e
- Inclination i
- Longitude of the ascending node Ω
- Argument of perigee ω
- True anomaly ν

Figure 4: Keplerian elements [7]

A S/C, whose orbital period is of the same duration as the Earth takes to rotate around its axis, is located on a so-called geosynchronous orbit. In general, the period is directly related to the semi-major axis and for a geosynchronous orbit, the period of 23h and 56min corresponds to $a_{GEO} \approx 42164$ km. Moreover, an orbit with these characteristics can have any eccentricity and inclination. If the path of the satellite is projected on the ground, the S/C will follow the



In reality, the S/C's mean longitude is not constant over time but drifts by the so-called *mean longitude drift rate*:

$$D = -\frac{3}{2} \frac{\delta a}{a_{GEO}} \quad (1)$$

We see that it often makes more sense to describe geostationary orbits using the so-called *synchronous* elements which are defined as a set of the following parameters:

$$[\lambda_m, D, e_x, e_y, i_x, i_y] = [\lambda_m, D, e, i]$$

Throughout this work study, a vector is denoted by a bold letter and scalar values by non-bold variables. Hence, \mathbf{e} and \mathbf{i} indicate respectively the eccentricity and inclination vector. \mathbf{e} represents a vector in the equatorial plane pointing towards the orbit's perigee with a magnitude of e while \mathbf{i} is the projection on the equatorial plane of the orbital pole, the axis perpendicular to the orbital plane.

$$\mathbf{e} = \begin{pmatrix} e \sin(\Omega + \omega) \\ e \cos(\Omega + \omega) \end{pmatrix} \quad \mathbf{i} = \begin{pmatrix} i \sin \Omega \\ -i \cos \Omega \end{pmatrix} \quad (2)$$

3.2.1 Mean and osculating elements

Considering the simplified case of only two objects in space, the S/C and Earth, and a symmetric gravitational effect as the only physical interaction between them, the S/C would follow a relative motion given by:

$$\ddot{\mathbf{r}} = -\mu \frac{\mathbf{r}}{r^3} \quad (3)$$

In this non-linear second order differential relation described in Equation 3, $\ddot{\mathbf{r}}$ represents the relative acceleration vector, \mathbf{r} and r the distance of the S/C relative to Earth in vectorial and scalar form, respectively. μ is the gravitational parameter of Earth. The two body problem

given in Equation 3 cannot be applied in reality. Firstly, under real conditions, it cannot be assumed that the mass is only concentrated in one point and secondly, the motion of a S/C is additionally affected by further perturbations described in subsection 3.5. Instead, the orbital elements can be either given in the form of *osculating* or *mean* elements. Osculating elements describe the motion on an osculating orbit, a two body trajectory that would be followed if the perturbations have been instantly switched off. At this instant the perturbed and the osculating orbit intersect, and the equation of motion becomes the same as for Keplerian orbits. That says that every point of the perturbed trajectory has its own osculating trajectory with a different set of osculating elements. The reason here is, that these elements are affected by the disturbing acceleration \mathbf{a} that extends the relative motion as follows:

$$\ddot{\mathbf{r}} = -\mu \frac{\mathbf{r}}{r^3} + \mathbf{a} \quad (4)$$

\mathbf{a} introduces secular¹, short and long period variations in the S/C's motion in addition to the two body acceleration. As illustrated in Figure 6, the osculating elements at t_i represents the true state of the S/C. If \mathbf{a} is removed then the osculating elements are constant over time, except for the anomaly. After a long elapsed time the secular perturbation becomes dominant over the periodic perturbations and influences the variation of the osculating elements the most.

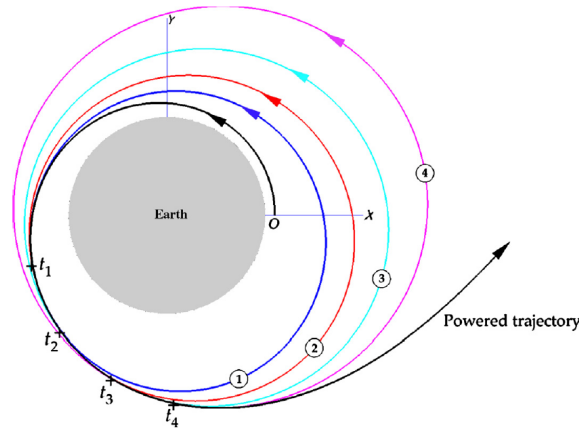


Figure 6: Osculating orbits 1-4 that correspond to the set of osculating elements at t_1 to t_4 . The S/C moves along the powered and spiral trajectory. The circled numbers on the osculating orbits mark the position of the orbits apogee.[9]

Furthermore, osculating elements are used in combination with numerical propagators but for long term propagation, the computation with these kind of models take too long and therefore, one instead prefers analytical or semi-analytical propagation models. For those models, one need to work with mean elements. Mean elements represent the "average" behaviour and are free from periodic effects. Consequently, they reveal the long-term behaviour of the S/C's orbit, only affected by secular perturbations, but do not represent the true position of the S/C at a specific time.[10] Furthermore, it is important to keep in mind, that there exists many kinds of mean elements.[5] We will see in practice that different conventions can lead to problems when converting elements from one into another model without the knowledge about the included perturbations.

As mentioned at the beginning of this section: A TLE stores the status of a S/C in the form of mean orbital elements where the periodic perturbations have been removed in a particular way. In order to process TLE mean elements and obtain maximum accuracy, it is of major importance that these periodic effects are reconstructed in the same manner. The analytical

¹secular perturbations mean long term and non- periodic variations in the classical orbital parameters

Simplified General Perturbations model SGP4 warrants this and computes the (osculating) state vector from the mean orbital elements given by the TLEs.[11] Besides from SGP4 there exist the predecessor SGP and the new models SGP8/SDP8. However, SGP4 is still commonly used but has been extended by SDP4 which includes the deep space effects, as the effect of lunar and solar gravitation, in case the orbital period exceeds a value of 225 min. In most literature, SGP4 is a term that combines the true SGP4, modelling the near Earth condition and the deep space extension SDP4. Table 1 represents the perturbations modelled by SGP4.

Secular Effects	Long period effects	Short period effects
<ul style="list-style-type: none"> • Atmospheric drag • Earth zonal harmonics (up to J4) • 3rd body (only in SDP4) • Resonance effects of Earth gravity (only in SDP4) 	<ul style="list-style-type: none"> • 3rd body (only in SDP4) • Earth gravity (up to J3) 	<ul style="list-style-type: none"> • Earth gravity (up to J2)

Table 1: Time scale of modelled perturbations in SGP4

In order to use TLE data for prediction of the S/C's motion, the SGP4 model transforms the mean elements into osculating ones by updating the elements by the secular effects before the long-period and short- period periodic terms are added. For this purpose, Hoots, Schumacher Jr, and Glover 2004 has published a detailed documentation about the evolution of SGP4 including all the equations.

Table 1 also shows that not all forms of perturbation are considered by the model which occur in reality. Among other aspects, the absence of the solar radiation pressure effects poses non-negligible error sources in the accuracy of SGP4. This introduces another kind of propagator: the Semi-analytic Tool for End of Life Analysis (STELA).

3.3 STELA

The Semi-analytic Tool for End of Life Analysis was implemented by the French Space Agency CNES in the frame of the French Space Act. It supports the computation of uncontrolled re-entry or the re-orbiting towards an appropriate disposal orbit while respecting the guidelines set in the French Space Operations Act. More precisely, the software enables the long term propagation of objects orbiting in LEO, GEO or GTO by means of a semi-analytic model. Furthermore, STELA differentiates between mean and osculating parameters. The semi-analytical model propagates the state of the S/C at each iteration step for which mean elements are used. In the following it is assumed that \mathbf{E}_n^{mean} denotes the mean orbital parameter state at time t_n and \mathbf{E}_{n+1}^{mean} the state one iteration later at t_{n+1} . \mathbf{E}_{n+1}^{mean} is then computed by means of the previous state and the derivative $\frac{d\mathbf{E}^{mean}}{dt}(\mathbf{t}_n)$ that sums up the contribution of all perturbation forces as follows:

$$\frac{d\mathbf{E}^{mean}}{dt} = \frac{d\mathbf{E}_{Kepler}^{mean}}{dt} + \frac{d\mathbf{E}_{Earth}^{mean}}{dt} + \frac{d\mathbf{E}_{Sun/Moon}^{mean}}{dt} + \frac{d\mathbf{E}_{drag}^{mean}}{dt} + \frac{d\mathbf{E}_{SRP}^{mean}}{dt} \quad (5)$$

Usually, all perturbing long- period periodic and secular effects have to be taken into account for the propagation model so that the STELA prediction is close to the real state of the S/C. However, after having analysed the eccentricity vector of several S/Cs, the long periodic contribution of the Moon with a period of one revolution (28 days) cannot be recovered. Consequently, it is assumed that during the generation of the SGP4 elements this periodic term was averaged. In order to remain consistent in the mean elements, the lunar gravity shall not be included in the force model for the propagation process with STELA.

As mentioned in subsection 3.2, mean elements are more suited for long term propagations where the short period terms has been analytically removed from the evolution. Consequently,

as seen in Equation 6, mean elements are defined as osculating parameters without short period perturbations.

$$\mathbf{E}_n^{osc} = \mathbf{E}_n^{mean} + \text{short periods} \quad (6)$$

On the other hand, for the propagation process a numerical integrator has been chosen based on a Runge Kutta method. The combination makes STELA a semi- analytic model.

In order to use TLE data for the propagation computation with STELA, we must first obtain the osculating parameters from the mean elements with SGP4 to recover the secular, long period and short period term which has been averaged in the TLE generation process. Since TLEs are generated in TEME, the resulting osculating elements need to be transformed in the appropriate frame of STELA which is the CIRF. Finally, for the propagation process itself, it is necessary to convert the osculating into mean elements which are derived by subtracting the short period terms from the S/C's state. [13]

3.4 Orbital manoeuvres

3.4.1 Manoeuvre requirements

In order to meet the requirements during the mission duration, a S/C will have to fire its on-board thrusters to change its current orbit. The most important requirement, on which this study is going to intensively focus on, is the station keeping(SK). The related manoeuvres are regularly performed to compensate natural and unnatural perturbations that cause the S/C to divert from its geostationary orbit. In addition, the S/C might perform station shifts, which are necessary in case the mission plan requires to change the mean longitude of the S/C during the mission. Furthermore, there also exist station acquisition manoeuvres which will bring the S/C to its desired orbit within the launch and early orbit phase (LEOP) and the so-called re-orbiting manoeuvres which are usually performed at the end of the mission to either raise or lower the orbit and manoeuvre the S/C outside the GEO rings according to international guidelines. We are not going to study station acquisitions because the TLE data within the LEOP are mostly disruptive and usually prone to aberrant values. Consequently, analysing manoeuvres within this period is very complex and requires more input data than just the publicly available TLE from the NORAD TLE catalogue. As previously, mentioned the focus is rather set on SK manoeuvres which are the most common manoeuvres performed throughout the lifetime of a S/C.

3.4.2 Station keeping routine

In order to keep the S/C under control the operator needs to follow the so- called station keeping control loop illustrated in Figure 7. This control loop consists of six programs: Tracking data processing, orbit determination, orbit prediction, orbit information, longitude and inclination station keeping. Within the process of tracking data, one collects the measurements of distance and direction of the S/C with respect to the ground stations. Furthermore, the measurements correspond to discrete epochs. Depending on the individual mission, more than one ground station can be involved. Since the raw data is noisy and afflicted with errors, the incoming data need to be smoothened, checked for quality, calibrated and time corrected. The orbit determination is very complex and prone to errors that could affect all the following steps and also our objective to detect manoeuvres. Within this program the orbital elements are computed for an epoch by least square fitting a numerically integrated arc over the preprocessed tracking data of the previous step. In order to guarantee high accuracy, this process is run regularly (weekly) and takes into account eight days of tracking data where one day overlaps with the consecutive interval of tracking. More important, it has to be run after a manoeuvre to evaluate the performance of the thrust and recalculate the orbit prediction. The orbit determination program further takes into account so- called auxiliary parameter which include the natural perturbation acceleration and the manoeuvre thrusts. The latter is computed by analysing the orbit just before and after the manoeuvre took place and deriving the $\Delta \mathbf{V}$ that caused the

discontinuity in the orbital evolution. The orbital prediction program will perform a propagation of the orbit starting from the set of orbital elements obtained from the orbital determination process. The orbit prediction is essential for the operator to know when he has to time a SK manoeuvre. In order to not violate the longitude and inclination deadband, he checks the predicted state of the orbit and initiates the station keeping program. After a manoeuvre, the orbit prediction program is repeated to take into account the changes. The orbit information then gives the orbital ephemeris of the S/C – Moon – Earth – Sun constellation in a compressed and convenient form.

In general, there exists two ways of scheduling a station keeping strategy:

- Perform manoeuvre one day before the longitude and inclination evolutions risk to violate the related deadbands. This strategy ensures the longest duration between two manoeuvres
- Follow a timed schedule so that the period between two manoeuvres is constant which simplifies the operational planning

Additionally, it is advantageous to schedule the inclination SK several days before the longitude SK in order to compensate the along track errors. This is for example the case for Himawari-8 which follows the strategy of a two burn manoeuvre to adapt the longitude drift and keep the eccentricity unchanged. The inclination cycle is schedule in such a way that the manoeuvre is performed one to two days before the EW manoeuvres.

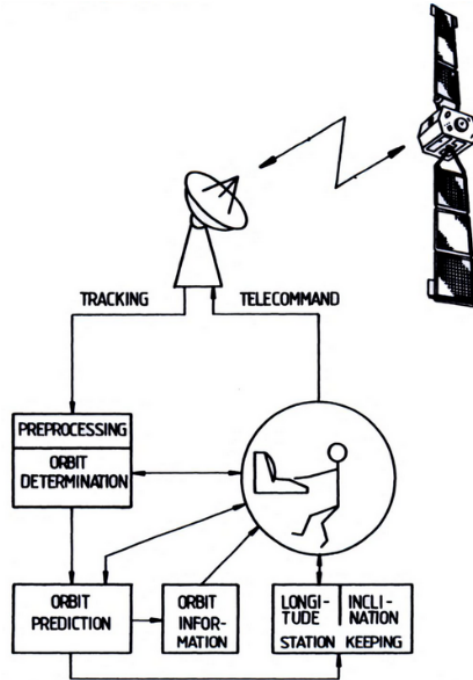


Figure 7: Illustration of SK control loop [8]

3.4.3 Types of manoeuvres

Soop [8] presents a detailed derivation of the linearised motion of a geostationary S/C using synchronous elements which were introduced in subsection 3.2. The advantage of linearisation is that it gives a simplified mathematical expression for the motion by adding linearly the different effects on the orbit. Therefore, we consider the motion with respect to Earth to be small and the S/C ideally at rest on its geostationary orbit. If the duration of the thrust Δt is short (≤ 1 h) in comparison to the orbital period, one can approximate the thrust as impulsive and add the velocity increment to the current state vector:

$$\Delta \mathbf{V} = \int_{t_b - \frac{\Delta t}{2}}^{t_b + \frac{\Delta t}{2}} \frac{\mathbf{F}}{m} dt \approx \frac{\mathbf{F}}{m} \Delta t \quad (7)$$

where t_b is the mid point time of the thrust. This means, if the state vector before the thrust has been (\mathbf{r}, \mathbf{V}) the next state vector after the thrust will be $(\mathbf{r}, \mathbf{V} + \Delta\mathbf{V})$.

In theory, there exists three types of manoeuvres because a thrust can be directed in three directions: orthogonal, tangential or radial to the satellite's orbit. However, radial thrusts are not common during a mission because they are not efficient and therefore costly, too. In Appendix B, this point is further explained by deriving the equations of the change in the orbital parameters due to a radial thrust. In either case, a manoeuvre thrust does not instantly affect the S/C's position but directly changes its velocity as seen in Equation 7. The change in the velocity components in radial, tangential and orthogonal directions are respectively denoted as: $\Delta V_r, \Delta V_t, \Delta V_o$. Considering the status of a S/C at thrust time t_b , the linearised equations of motion become:

$$0 = \Delta r = -A \left(\frac{2}{3} \Delta D + \Delta e_x \cos s_b + \Delta e_y \sin s_b \right) \quad (8)$$

$$0 = \Delta \lambda = \Delta \lambda_0 + \Delta D (s_b - s_0) + 2\Delta e_x \sin s_b - 2\Delta e_y \cos s_b \quad (9)$$

$$0 = \Delta \theta = -\Delta i_x \cos s_b - \Delta i_y \sin s_b \quad (10)$$

$$\Delta V_r = V (\Delta e_x \sin s_b - \Delta e_y \cos s_b) \quad (11)$$

$$\Delta V_t = V (\Delta D + 2\Delta e_x \cos s_b + 2\Delta e_y \sin s_b) \quad (12)$$

$$\Delta V_o = V (\Delta i_x \sin s_b - \Delta i_y \cos s_b) \quad (13)$$

where s_b is the sidereal angle at the thrusting time and D the drift rate. $\Delta \theta$ expresses the change in the latitude that depends on the change in the inclination Δi . The subscript "0" denotes all parameters at $t = t_0$. This linearisation is only justified for ΔV s in the range of 0.1 to 50 ms^{-1} when the thrust is much smaller than the orbital velocity (3 km s^{-1}). A detailed derivation of these equations is given by Soop [8] and will not be further explained in the scope of this work. Instead, we will apply these equation to the different types of manoeuvres in order to find an expression for the change in the orbital elements.

In GEO, one usually comes across orthogonal or tangential manoeuvres. Thrusts that result in a force orthogonal to the orbital plane are generally called out-of-plane or north- south (NS) manoeuvres. They change the inclination of the orbit and the ascending node but consume a high amount of fuel. The inclination of a GEO satellite is ideally at 0° , however, the influences of Sun's and Moon's attraction as well as the zonal terms of Earth's gravity keep perturbing the inclination vector. As a result, inclination SK manoeuvres have to be regularly performed and they need to be optimized to also keep the fuel consumption as low as possible.

In contrast to the NS thrusts, there exists east- west (EW) manoeuvres which generate a force tangential to the orbital plane. They affect the longitude drift rate and the eccentricity of the orbit. In the first order approximation, the longitude drift is perturbed mainly by the tesseral contribution of Earth's potential field while the eccentricity vector is influenced by the solar radiation pressure and slightly by the solar and lunar attractions. In the following, we will focus more on the theory of in-plane and out-of-plane manoeuvres, which are performed to counteract these perturbations, and derive the solution of the equations of motion.

a) Inclination manoeuvre

In subsection 3.2 we have given the definition of the two dimensional inclination vector.

$$\mathbf{i} = \begin{pmatrix} i \sin \Omega \\ -i \cos \Omega \end{pmatrix} \quad (2)$$

where i represents the angle between the equatorial plane and the orbital plane and Ω marks one of the node where the orbit intersects with the equatorial plane. In case of a plane change the angle between the old and new orbital plane is approximately $\Delta V/V$. The position where the thrust will be fired is given by the sidereal angle s_b marking one

of the points where the new intersects with the old orbit. The change of two dimensional inclination with one thrust is then given by:

$$\Delta \bar{i} = \frac{\Delta V}{V} \begin{bmatrix} \sin s_b \\ -\cos s_b \end{bmatrix} \quad (14)$$

In order to derive the change in the latitude θ , we need to know that generally, θ is dependent on the sidereal angle s :

$$\theta = i \sin(s - \Omega) \quad (15)$$

In case of an inclination change, $\Delta\theta$ can be derived in a similar way as Δi :

$$\Delta\theta = \frac{\Delta V}{V} \sin(s - s_b) \quad (16)$$

In order to obtain the evolution of the S/Cs latitude and inclination over a continuous thrust, we consider that the burn is composed of an infinite number of thrusts $(\Delta V / \Delta s) ds_b$ at different positions s_b . Accordingly, we integrate over the duration of the thrust starting from s_1 to s_2 or the current sidereal angle s :

$$\Delta\theta = \frac{\Delta V}{V \Delta s} \int_{s_1}^{s_2} \sin(s - s_b) ds_b = \frac{\Delta V}{V \Delta s} [\cos(s - s_2) - \cos(s - s_1)] \quad (17)$$

$$\Delta \bar{i} = \frac{\Delta V}{V \Delta s} \begin{bmatrix} \cos s_1 - \cos s_2 \\ \sin s_1 - \sin s_2 \end{bmatrix} = \frac{\Delta V}{V \Delta s} 2 \sin \frac{s_2 - s_1}{2} \begin{bmatrix} \sin \frac{(s_1 + s_2)}{2} \\ -\cos \frac{(s_1 + s_2)}{2} \end{bmatrix} \quad (18)$$

with $s_1 \leq s \leq s_2$.

b) Longitude manoeuvre

A tangential thrust can be performed either as an eastward thrust ($+\Delta V$) or as a westward thrust ($-\Delta V$).

Types		
Eastwards	$+\Delta V$	<ul style="list-style-type: none"> • ΔV raises orbit everywhere besides from there, where the thrust has been fired • Position of thrust becomes new perigee • Apogee on the other side is raised by an increment proportional to ΔV
Westwards	$-\Delta V$	<ul style="list-style-type: none"> • ΔV lowers orbit everywhere besides from there, where the thrust has been fired • Position of thrust becomes new apogee

Table 2: Effects of east and west manoeuvres

As mentioned previously, the tangential thrust can be considered as an instantaneous impulse that immediately changes the velocity of the S/C but not its position. When a single longitudinal manoeuvre is performed, the conditions of Equation 8 to Equation 13 simplify to:

$$0 = \Delta r = -A \left(\frac{2}{3} \Delta D + \Delta e_x \cos s_b + \Delta e_y \sin s_b \right) \quad (19)$$

$$0 = \Delta \lambda = \Delta \lambda_0 + \Delta D (s_b - s_0) + 2\Delta e_x \sin s_b - 2\Delta e_y \cos s_b \quad (20)$$

$$0 = \Delta V_r = V (\Delta e_x \sin s_b - \Delta e_y \cos s_b) \quad (21)$$

$$\Delta V_t = V (\Delta D + 2\Delta e_x \cos s_b + 2\Delta e_y \sin s_b) \quad (22)$$

and the solutions for the four elements ($\Delta\lambda_0$, ΔD , Δe_x and Δe_y) become:

$$\Delta\lambda_0 = \frac{3\Delta V}{V} (s_b - s_0) \quad (23)$$

$$\Delta D = -\frac{3\Delta V}{V} \quad (24)$$

$$\Delta\bar{e} = \bar{e}_{new} - \bar{e}_{old} = \frac{2\Delta V}{V} \begin{bmatrix} \cos s_b \\ \sin s_b \end{bmatrix} \quad (25)$$

Equation 24 shows that the drift rate is always oriented opposite to the manoeuvre push, for example in case an eastward manoeuvre has been performed the drift rate would give a westwards drift and vice versa. This is due to the fact that during an eastward thrust the semi major axis is lifted up resulting in an increased orbital period. Consequently, the mean orbital velocity decreases with respect to Earth's rotation and leads to a westward drift. The similar case is happening when a negative ΔV is applied. Here, the period decreases resulting in a mean east drift.

By applying Equation 24 one can derive the expression of the semi major axis change:

$$\Delta a = a_{new} - a_{old} = -\frac{2A}{3} \frac{\Delta V}{V} = \frac{2}{\Psi} \Delta V \quad (26)$$

where Ψ is Earth's angular velocity.

Applying Equation 25 to Equation 19 reveals an expression for the change of the S/Cs position Δr in terms of the sidereal angle.

$$\Delta r = \frac{2\Delta V}{\Psi} [1 - \cos(s - s_b)] \quad (27)$$

A similar expression can be found for the longitude change when we apply Equation 23, Equation 24 and Equation 25 to Equation 20:

$$\Delta\lambda = \frac{\Delta V}{V} [4 \sin(s - s_b) - 3(s - s_b)] \quad (28)$$

c) Multiple manoeuvres

As seen in the preceding point, the problem of a single manoeuvre is the coupling between the eccentricity vector and the longitude drift rate. One cannot choose independently how to change one parameter without affecting the other. However, by performing multiple tangential thrusts, one can generate several combinations of the longitude drift rate and the eccentricity, independently of each other. The most common multiple in plane manoeuvre is the *two burn longitude manoeuvre* where both manoeuvres are separated by half a revolution (or half a sidereal day). To describe the effects of a , D and e , it is necessary to add the velocity increments ΔV_1 and ΔV_2 due to the burns in Equation 24, Equation 25 and Equation 26 revealing:

$$\Delta D = -\frac{3(\Delta V_1 + \Delta V_2)}{V} \quad (29)$$

$$\Delta\bar{e} = \frac{2(\Delta V_1 - \Delta V_2)}{V} \begin{bmatrix} \cos s_1 \\ \sin s_1 \end{bmatrix} = \frac{2(\Delta V_2 - \Delta V_1)}{V} \begin{bmatrix} \cos s_2 \\ \sin s_2 \end{bmatrix} \quad (30)$$

In principle we can consider the manoeuvre at $s_1 \leq s \leq s_2$ as a single in- plane manoeuvre, but, as soon as $s > s_2$, the effect of two ΔV act on the orbital evolution. From that moment Δr and $\Delta\lambda$ are given by:

$$\Delta r = \frac{2}{\Psi} [\Delta V_1 - \Delta V_2 - (\Delta V_1 - \Delta V_2) \cos(s - s_2)] \quad (31)$$

$$\Delta\lambda = \frac{1}{V} (\Delta V_1 - \Delta V_2) [4 \sin(s - s_2) - 1, 5\pi] - \frac{3}{V} (\Delta V_1 + \Delta V_2) \left(s - s_1 - \frac{\pi}{2}\right) \quad (32)$$

In case one wants to change D without changing \mathbf{e} , the two thrust need to have the same magnitude and direction because then the effect of $\Delta \mathbf{e}$ gets cancelled. This is famously known as a classical Hohmann transfer. In case one wants to change the eccentricity but not the longitude drift rate the same thrust in magnitude but with opposite signs have to be applied. If the east thrust has been applied first and the west thrust as the second half a revolution later, we will see that the mean longitude of the new orbit is shifted by $-3\pi\Delta V_1/V$ to the west when $\Delta V_2 = -\Delta V_1$. If the mean longitude shift is not wanted, it can be suppressed by performing a three burn manoeuvre (east - west - east), where the two east thrusts are of the same magnitude as the single west burn. Here the first thrust raises the orbit which will decrease with the following west burn and increase with the final thrust to get to the same mean longitude as inertially. Δr and $\Delta \lambda$ are then given by:

$$\Delta r = \frac{2}{\Psi} [\Delta V_1 + \Delta V_2 + \Delta V_3 + (\Delta V_1 - \Delta V_2 + \Delta V_3) \cos(s - s_2)] \quad (33)$$

$$\begin{aligned} \Delta \lambda = & \frac{3\pi}{V} (\Delta V_3 - \Delta V_1) - \frac{3}{V} (\Delta V_1 + \Delta V_2 + \Delta V_3) (s - s_2) \\ & - \frac{4}{V} (\Delta V_1 - \Delta V_2 + \Delta V_3) \sin(s - s_2) \end{aligned} \quad (34)$$

3.5 Effects of perturbations on spacecrafts

As stated in subsubsection 3.4.1, station keeping thrusts are required since the S/C is subject to natural and unnatural perturbations but needs to maintain the desired orbit. The design of the S/C sometimes permits the installation of the thrusters at the desired place in order to produce to most efficient thrust. Instead, one needs to find a compromise with the other equipment (such as payload instruments, solar panels or antennas) and sometimes the thrusters are mounted in such a way that the force vector does not pass through the mass centre. Consequently, this will result in a torque and also, decreases the efficiency of the manoeuvre that may require additional manoeuvres to compensate. Besides from thrusting errors, there exists several natural sources of perturbations which have been briefly summarized in Table 3. In the following we are going to focus on the effects of the perturbing forces on the S/C in order to understand what drives the need of performing SK manoeuvres.

Perturbations	Effects
Non spherical gravity field of Earth <ul style="list-style-type: none"> • Tesserall terms • Zonal terms 	D \mathbf{i} (slightly), a
Three body system	\mathbf{i}, \mathbf{e} (slightly)
Solar radiation pressure (SRP)	\mathbf{e}

Table 3: Overview of perturbations

3.5.1 Non-spheric Earth potential

According to Newton, every mass M_1 attracts every other mass M_2 by a force g which is proportional to the product of the interacting masses. Considering, that $M_1 \gg M_2$, the force towards the central mass is defined as:

$$\mathbf{g} = -\frac{GM_1}{r^2} \hat{\mathbf{r}} \quad (35)$$

where G is the gravitational constant and $\hat{\mathbf{r}}$ expresses the direction from the central mass towards M_2 . Accordingly, M_2 has a gravitational potential energy R with respect to its position in the gravity field of M_1 . It follows that a work is done on M_2 by the gravitational force in order to move the smaller mass from its current position \mathbf{r}_{ref} to \mathbf{r} , towards the direction of the central mass. Furthermore, we assume that $r_{ref} = \infty$.

$$R = \int_{\mathbf{r}_{ref}}^{\mathbf{r}} \mathbf{g} \cdot d\mathbf{r} = - \int_{\mathbf{r}_{ref}}^{\mathbf{r}} \frac{GM_1}{r'^2} \hat{\mathbf{r}} \cdot d\mathbf{r} = GM_1 \int_{\infty}^r \frac{1}{r'^2} dr' = -\frac{GM_1}{r} \quad (36)$$

It should be noted that $\hat{\mathbf{r}}$ and \mathbf{r} point in opposite direction since \mathbf{r} shows how M_2 moves from its current position towards the gravitational well.

Moreover, it follows from Equation 36 that the gravitational potential is the integration of force over space, consequently, the gravitational force must be the spatial derivative of the potential and Equation 35 can be extended as follows:

$$\mathbf{g} = \frac{\partial}{\partial \mathbf{r}} \left(\frac{GM}{r} \right) = -\frac{\partial}{\partial \mathbf{r}} U = -\mathbf{grad} R \equiv -\nabla R \quad (37)$$

The negative sign on the right side of Equation 37 shows that M_2 further gets accelerated towards the centre mass while its potential energy decreases. In other words, the minus guarantees that the gradient is directed opposite to $\hat{\mathbf{r}}$, in the direction of decreasing r . Points of constant R are forming a surface known as equipotential. In case M_1 is spherically symmetric, the equipotential surface would be a sphere and every point on it encounters a gravitational force that is directed towards the centre of this sphere. However, Earth's form does neither represent a sphere nor is its mass symmetrically distributed. In order to accurately model the Earth's gravity, its potential is expanded in a series. This study will not focus on the derivation of the mathematical model of R , but we will assume that Earth's gravitational potential is given by:

$$R = \frac{\mu}{r} + \mu \sum_{l=2}^L \sum_{m=0}^l \frac{R_e^l}{r^{l+1}} P_{lm}(\sin \theta) (C_{lm} \cos m\lambda + S_{lm} \sin m\lambda) \quad (38)$$

where R_e is the radius of the Earth. The potential function is defined by a series development in spherical harmonics. The sets of coefficients have been derived taking into account satellite measurements and the analysis of the perturbations on their orbits. P_{lm} denote the corresponding Legendre functions of degree l and order m . Considering that the Earth is non-spherical introduces the angles θ and λ that denotes the spherical coordinates of the S/C. The C terms with $m = 0$ denote the zonal terms and represent the expansion that is rotationally symmetric caused by Earth's flatness. Hence the gravitational potential in this sense would be independent of λ . The tesseral terms, the terms where $m \leq l$, introduce the gravitational potential as both latitude and longitude dependent caused by the unsymmetrical mass distribution of Earth's body. The tangential component of the gravitational acceleration due to the tesseral terms plays a major role with respect to the longitude drift. The disturbing acceleration is dominated by the coefficients with $l = m = 2$ and results in a potential given by:

$$\begin{aligned} R_{22} &= \frac{\mu}{r} \left(\frac{R_e}{r} \right)^2 P_{22}(\sin \theta) (C_{22} \cos 2\lambda + S_{22} \sin 2\lambda) \\ &= 3 \cdot \frac{\mu}{r} \left(\frac{R_e}{r} \right)^2 \cos^2 \theta \cos [2(\lambda - \lambda_{22})] \end{aligned} \quad (39)$$

where P_{22} denotes the Legendre function of second degree and second order. λ_{22} expresses a term combining the geopotential coefficients as:

$$\lambda_{22} = \frac{1}{2} \arctan \frac{S_{22}}{C_{22}} \quad (40)$$

Assuming that θ becomes approximately zero for GEO satellite, the acceleration in Equation 39 becomes sinusoidally dependent on the longitudes with four nodes. The four nodes mark the longitudinal position at which the S/C does not encounter an acceleration and therefore, remains at rest. Two of them are so-called *stable* equilibrium points meaning that a S/C that is slightly dislocated from these nodes will experience a drift that brings it back to the stable points. That means that a GEO satellite at any longitude will accelerate towards the closest stable point and swings around this node like a pendulum. In contrast to this, the other two equilibrium points are known as *unstable* points. Unlike the stable nodes, the S/C would directly drift away in either direction, if it is not exactly located at the unstable points.[8]

- stable points: 75.1°E and 105.3°W
- unstable points: 11.5°W and 161.9°E

Due to the presence of these equilibrium points, the S/C drifts away from its mean longitude and the satellite's operator need to perform SK manoeuvres in order counteract the longitudinal acceleration caused by the tangential component of the tesseral gravitational attraction B :

$$\frac{d^2\lambda}{dt^2} = -\frac{3}{A}B \quad (41)$$

Considering, that B is constant within a small interval around the mean longitude, we can double integrate Equation 41 and obtain the mean longitudinal motion. The evolution of the longitude follows a parabolic curve which is opened towards the direction of the nearest stable point. The parabolic behaviour can be compared with the projectile motion where a projectile is tossed up and moves along a parabolic curve under the influence of gravity. In the case of the longitudinal motion, the toss corresponds to the manoeuvre thrust acting against the acceleration caused by B .

3.5.2 Solar Radiation Pressure

Even though electromagnetic radiation is massless, it can still transfer momentum when it moves with speed of light but hits an object on its path. The exerted pressure is called *Solar Radiation Pressure* (SRP). The SRP that acts on an orthogonal plane close to Earth has a magnitude of

$$P = 4.56 \times 10^{-6} \text{ N m}^{-2}$$

This electromagnetic radiation pressure generates a force on the S/C which is proportional to its cross- section S :

$$F = PS(1 + \epsilon) \quad (42)$$

where ϵ is the surface reflectivity coefficient. The acceleration is always directed away from the Sun and depends on the cross-section to mass ration (S/m) and ϵ .

$$\frac{F}{m} = P(1 + \epsilon) \frac{S}{m} \quad (43)$$

Depending on the cross- section and the reflectivity of the S/C, the magnitude of this acceleration on a GEO satellite is usually of the order of 10^{-7} m s^{-2} . Since it is difficult to express the varying cross- section and reflectivity of the S/C, it is common to model the acceleration with one single parameter, the effective cross- section to mass ratio defined as:

$$\sigma := \left(\frac{S}{M} \right)_{eff} = \frac{S(1 + \epsilon)}{m} \quad (44)$$

The only orbital element which is affected by the solar radiation pressure is e because the mean effect on a and i vanishes when we average over one sidereal day. Consequently, we will derive the mean motion of the eccentricity vector encountered by SRP.

Assuming that the S/C is positioned at the sidereal angle s , the tangential and radial component of the velocity due to the radiation pressure differential dV is expressed as:

$$dV_t = \sin(s - s_s) dV \quad dV_r = -\cos(s - s_s) dV \quad (45)$$

with s_s as the sidereal projection of the Sun on the orbital plane. Recalling the equations of an eccentricity change during a tangential and a radial burn, as presented in subsubsection 3.4.3 and Appendix B, results in the following differential for e in this scenario:

$$\frac{de}{dt} = \frac{2}{V} \begin{bmatrix} \cos s_b \\ \sin s_b \end{bmatrix} \frac{dV_t}{dt} + \frac{1}{V} \begin{bmatrix} \sin s_b \\ -\cos s_b \end{bmatrix} \frac{dV_r}{dt} \quad (46)$$

By integrating Equation 46 over one sidereal day, we retrieve the mean drift rate of \mathbf{e} given as:

$$\frac{\delta \mathbf{e}}{\delta t} = \frac{3P\sigma}{2V} \begin{bmatrix} -\sin s_s \\ \cos s_s \end{bmatrix} \quad (47)$$

This shows that the mean drift goes in the direction $+90^\circ$ from the Sun and it changes throughout the years because of its varying sidereal angle s_s .

4 Data pre-processing

As previously mentioned, the input data of our study are TLEs downloaded from the catalogue which can be accessed through www.space-track.org. The mean elements stored in the TLEs are called mean SGP4 elements because the periodic variations have been averaged in a particular way.[14] The SGP4 model is used to reconstruct the osculating elements from the mean SGP4 elements. Therefore, the model propagates the state to each TLE epoch taken into account the perturbation summarized in Table 1. In order to finally retrieve the osculating quantities, the short- period periodics are added to the orbital elements. From Hoots, Schumacher Jr, and Glover [12], we know that only Earth's J2 gravitational contribution is considered as short period periodic effect. Even though we have discussed in subsection 3.2.1 that osculating elements represent the true state of the S/C, the elements retrieved after the SGP4 conversion are not the "real osculating elements". The reason for this is that other short- period effects like the third body contribution have been neglected. Even though the J2 gravitational potential is the most important short term variation, the derived orbital state is only close to the osculating state.

As previously discussed, we are not using SGP4 for any of our propagation studies. Consequently, the mean SGP4 elements need to be converted into STELA elements while being aware of what effect is exactly considered as short- periodic term in SGP4. Therefore, the mean SGP4 elements are firstly converted to osculating elements with the SGP4 model by adding the short terms variations to the orbital parameters. In order to make the conversion to STELA, all the orbital parameters are transformed at each TLE epoch with respect to the force model in STELA. The mean STELA elements are then obtained by removing the J2 gravitational terms from osculating parameters. It is of major importance to remain consistence in the transformation *mean SGP4* \rightarrow *osculating* and in the conversion *osculating* \rightarrow *mean STELA*. That says that only those contribution shall be removed or added to the orbital parameters which has been considered as short periodic variation in the very beginning when the osculating elements were generated. If other forces are additionally taken into account for the transformations, we will remove or add artificial short term variations to the elements and end up with wrong mean STELA elements.

Besides from the correct conversion of the element's nature, we must ensure that the frames are correctly transformed, too. The TLE's represent the state of the orbit in the TEME frame but the integration frame in STELA is CIRF. Figure 8 illustrates the steps for the conversion of the element's nature and the transformation into the appropriate reference frame.

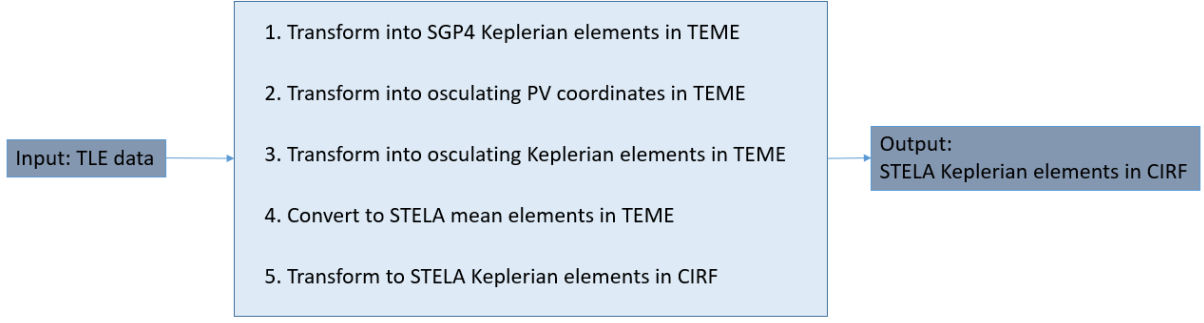


Figure 8: Summary of the algorithm of the mean element conversion from mean SGP4 in the TME frame to mean STELA elements in CIRF

5 Estimation of the area to mass ratio

From subsection 3.4.3, we recall that a single longitude thrust mainly affects the semi-major axis, the longitudinal drift and the eccentricity vector. Consequently, these parameters are interesting to analyse and their natural behaviour should be understood in order to detect any conspicuous anomalies that could have been caused by a manoeuvre. During its natural evolution, the S/C encounters several perturbation forces that has been explained in subsection 3.5. One of the perturbing forces is driven by the radiation pressure exerted by our Sun. The magnitude of the solar radiation pressure P introduced in subsection 3.5.2 is in fact a function of the distance to the Sun. In GEO, this perturbation cannot be neglected and depending on the surface- to- mass ratio (S/M) the related acceleration is generally of the order of 10^{-7} m s^{-2} . [8] Usually, there is no way to know the S/M in advance, for example from a database or from the TLE itself. However, OPERA already provides an algorithm to estimate the S/M affected by the SRP but our tests have shown that the estimations comes with a large error which would affect our results in the manoeuvre detection, too. Furthermore, the existing algorithm relies on a polynomial fit over the observation data without any physical explanation why the data should behave like a polynomial curve. For a more detailed analysis, the theory of the existing S/M in OPERA is presented in the user manual. [15] In order to continue with the study, we need to develop a more precise algorithm for the estimation of the S/M. The new method is based on the Levenberg Marquardt algorithm that treats the problem of finding the best S/M as a least square problem. The objective is to find the best estimation of the S/M by analysing the influence of the SRP on the behaviour of the eccentricity vector. This correlation is valid, because the solar radiation acceleration is proportional to the S/M and the only orbital parameters affected by this perturbation are the components of the eccentricity e_x and e_y .

The least square (LS) problem is given by:

$$\arg \min_{\beta} S(\beta) \equiv \arg \min_{\beta} \sum_{i=1}^m [y_i - f(x_i, \beta)]^2 \quad (48)$$

$$x \in \mathbb{R}^2 \quad f(x_i, \beta), y \in \mathbb{R}^m$$

General	In the case of S/M estimation
x_i, y_i ... set of (in-)dependent variables	x_i ... current epoch y_i ... current TLE state ($e_{x,TLE}, e_{y,TLE}$)
β ... parameters of the model curve ($n \times 1$)	β ... current S/M estimation (1×1)
$f(x_i, \beta)$... model curve	$f(x_i, \beta)$... state predicted by STELA ($e_{x,STELA}, e_{y,STELA}$)
m ... size of the empirical set	m ... number of TLEs in TLE history
S ... squares of deviation	S ... squares of deviation between TLE and STELA

Table 4: Meaning of the variables in Equation 48

As shown in Table 4 we will use STELA in order to make a prediction of the eccentricity state with respect to the current S/M estimation β . β is then considered as a good estimation, if the square of the deviation between the expected evolution and the observation has converged towards the minimum. To find this minimum, β is updated by an increment δ in each iteration. $f(x_i, \beta + \delta)$ is then approximated by a linearisation as follows:

$$f(x_i, \beta + \delta) \approx f(x_i, \beta) + \mathbf{J}_i \delta \quad (49)$$

where

$$\mathbf{J}_i = \frac{df(x_i, \beta)}{d\beta} \quad (50)$$

\mathbf{J}_i denotes the gradient of the function f . Using Equation 48, the next iteration step is approximated by:

$$S(\beta + \delta) \approx \sum_{i=1}^m [y_i - f(x_i, \beta) - \mathbf{J}_i \delta]^2 \quad (51)$$

Using the vector notation, Equation 51 can be rewritten as:

$$S(\beta + \delta) \approx \|\mathbf{y} - \mathbf{f}(\beta) - \mathbf{J}\delta\|^2 \quad (52)$$

\mathbf{J} is the Jacobian matrix with the dimension of $(m \times n)$, where n is the size of β denoting the number of parameters. $\mathbf{f}(\beta)$ and \mathbf{y} are vectors whose i -th component represent $f(x_i, \beta)$ and y_i , respectively.[16] For the computation of the minimum we need to take the derivative of $S(\beta + \delta)$ with respect to δ and set it equal to zero. That will result in the following relation:

$$(\mathbf{J}^T \mathbf{J}) \delta = 2\mathbf{J}^T [\mathbf{y} - \mathbf{f}(\beta)] \quad (53)$$

The set of linear equations to solve δ presented in Equation 53 is known as the Gauss-Newton algorithm. In the Levenberg Marquardt algorithm, the equations are extended by a damping contribution:

$$(\mathbf{J}^T \mathbf{J} + k\mathbf{I}) \delta = 2\mathbf{J}^T [\mathbf{y} - \mathbf{f}(\beta)] \quad (54)$$

where k denotes the damping factor and \mathbf{I} the identity matrix. As indicated in Figure 9, the adjustment of k influences the convergence and brings the solution closer to the Gauss-Newton algorithm, in case S and the residual reduce to rapidly, so that one need to decrease k . Vice versa, k is increased if the reduction is too slow and the solution should rather be closer to the gradient descent direction.[16] That says that with each iteration, k is adjusted in such a way until a solution is found. The conditions for finding the optimal S/M is fulfilled as soon as δ is sufficiently small, or S and the residual are low enough.

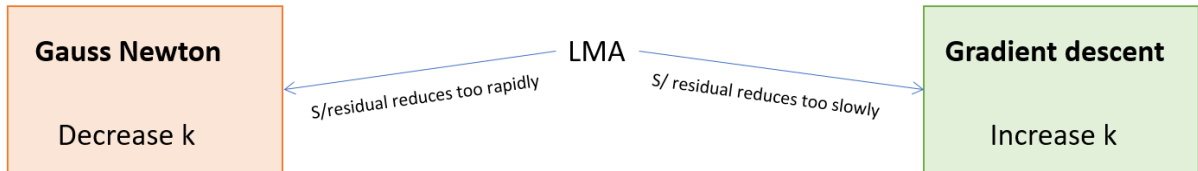


Figure 9: k is adjusted after each iteration and the result either approaches the Gauss-Newton solution or the solution of the gradient descent

5.1 Implementation

The Levenberg Marquardt optimizer is already implemented in PATRIUS library by CNES. In order to use the optimizer, we need to define the conditions adapted to our problem. In the preceding subsection, the objective was to solve the LS problem of Equation 48 and thereby minimize the residual between the predictions of dynamical model and the observation. However, in our implementation we will minimize the residual between a so-called *target* and the difference between dynamical model and observation $\mathbf{f}(\boldsymbol{\beta})$. The target represents the objective to minimize the residuals and it is initialized as a vector of zeros with a dimension of $2m \times 1$. The reason of the factor 2 results from the fact that we combine the x - and y - component of the eccentricity vector into one vector. Hence the size of target must be two times the number of TLEs in the time history.

Two things needed to be implemented in order to use the Levenberg Marquardt optimizer for our problem: The calculation of the residuals between target and $\mathbf{f}(\boldsymbol{\beta})$ and the computation of the Jacobian matrix \mathbf{J} .

a) Calculation of the residual between target and $\mathbf{f}(\boldsymbol{\beta})$

For the calculation of the error between the observed eccentricity evolution and the predicted evolution by STELA, the epoch times must correlate. That means that for the STELA propagation, we need to propagate the state starting from the first TLE towards all the TLE epochs. Consequently, the propagation duration is newly set for every TLE and we finally retrieve the propagated state at every epoch in the time history. For the propagation, only the force model of the zonal and tesseral attraction, as well as of the Sun's gravitation are taking into account but not the perturbations due to the atmospheric drag or the short periodic terms of Moon's gravity. At the altitude of GEO satellites the density of the atmosphere becomes negligible and justifies the disregard of the drag model. Furthermore, we must not take the Moon's gravitational influence into account because within the TLE generation process, the Moon's contribution is averaged over one revolution, hence, over 28 days. Consequently, this period effect of the Moon must be excluded from the modelling of the perturbations.[17] In the end, at each epoch i within the time history the resulting difference between STELA and TLE is given by:

$$e_{x,res_i} = e_{x,TLE_i} - e_{x,STELA_i} \quad e_{y,res_i} = e_{y,TLE_i} - e_{y,STELA_i} \quad (55)$$

The vector of the error is defined as:

$$\mathbf{f}(\boldsymbol{\beta}) = \begin{pmatrix} e_{x,res_1} \\ e_{y,res_1} \\ \vdots \\ e_{x,res_m} \\ e_{y,res_m} \end{pmatrix} \quad (56)$$

The residual is then the difference between the target vector and the error vector.

b) Computation of the Jacobian matrix \mathbf{J}

The Jacobian matrix has been introduced in subsection 3.5 as a matrix that stores the gradient of function f . As previously stated, f is no longer the state predicted by the dynamical model but rather the error between STELA and the observations. Hence, \mathbf{J} stores the gradient of this error with respect to all the variables of $\boldsymbol{\beta}$. Since in our case $\boldsymbol{\beta}$ only consists of the S/M, the dimension of the Jacobian matrix is $2m \times 1$, where the factor of 2 again denotes the combination of both components of vector \mathbf{e} . Consequently, for our

problem, \mathbf{J} is defined as:

$$\mathbf{J} = \begin{pmatrix} \frac{\partial e_{x,res1}}{\partial \beta} \\ \frac{\partial e_{y,res1}}{\partial \beta} \\ \vdots \\ \frac{\partial e_{x,resm}}{\partial \beta} \\ \frac{\partial e_{y,resm}}{\partial \beta} \end{pmatrix} \quad (57)$$

The differentials in Equation 57 are computed with:

$$\frac{\partial e_{x/y,res}(\beta)}{\partial \beta} = \frac{e_{x/y,res}(\beta + h\beta) - e_{x/y,res}(\beta - h\beta)}{2h\beta} \quad (58)$$

where h is set to 0.05.

The Levenberg Marquardt optimizer converges to a solution of the LS problem and we will then consider this solution as the S/M of the analysed S/C. It should be noted that the estimated S/M is no geometrical quantity. That means that this value does not correspond to the size of any surface on the S/C, nor does it represent the average cross-section of the S/C based on the assumption of random tumbling in all directions. The quantity returned in our algorithm corresponds to the average cross-section which encounters solar radiation over the user-defined simulation duration. This radiation generates a force acting on the effective cross-section that is perpendicular to the Sun's direction and builds up the SRP that perturbs the eccentricity behaviour of the S/C. Hence, the effective cross-section depends on the current position of the Sun relative to the S/C, which means that when the S/C is in eclipse the effective cross-section is zero and no SRP acts on the satellite. Nevertheless, the estimated value in our algorithm is the averaged behaviour of the effective cross-section over the duration of the simulation.

5.2 Tests and verification

In order to evaluate the performance of our algorithm of estimating the S/M using the Levenberg Marquardt optimizer, we are going to compare the results with the old estimation algorithm. Both algorithms are applied to non-operating GEO satellites which have reached their end of life (EOL) in the past. It is important to only analyse objects which are not manoeuvring because our algorithm adapts the S/M estimation in accordance to the observed eccentricity vector evolution. Thereby, it does not take into account the contribution of any unnatural accelerations. Consequently, the presence of thrusts within the simulation interval will perturb the behaviour of the eccentricity and the resulting S/M estimation cannot be trusted. Both algorithms were applied to ten randomly selected non-operational satellites:

- Meteosat 2 - EUMETSAT (12544)
- DFS Kopernikus 1 - Germany (20041)
- INSAT 1D - India (20643)
- Inmarsat 2 F2 - GB (21149)
- Spacenet 4 - USA (21227)
- Telecom 2A - France (21813)
- Cosmos 2319 - Russia (23653)
- Galaxy IVR - USA (26298)
- Ekspress MD1 - Russia (33596)
- AMOS 5 - Israel (37950)

The principle of the tests is to compute the S/M with each algorithm and plot the evolution of the STELA propagation using the estimated S/Ms. The propagated evolution that is closer to the observed data derived from the TLEs is considered to be more accurate. It also means that the S/M related to that propagation is more reliable.

For the S/M estimation, a simulation duration of 13 and 30 days was set in order to take a sufficient amount of data to fit the estimation of the observation. That means that for each S/C we retrieved four estimation for the S/M: two correspond to the old method with a simulation duration of 13 and 30 days and the other two values were computed with the new algorithm. In both algorithms the returned S/M was given in $\text{m}^2 \text{kg}^{-1}$ and the values were then handed over to

STELA for the propagation process. For the propagation, we start from a common time epoch and propagated the state towards each consecutive epoch in the TLE history over a duration of more than five months. In order to visually compare the predicted evolution by STELA, both propagations are plotted together with the true eccentricity evolution in scilab. Figure 11 and Figure 13 show the results for the S/M estimation of DFS Kopernikus 1 and Telecom 2A, respectively. The black curve shows the observed eccentricity vector derived from the TLEs, the green curve corresponds to the S/C estimation performed with the new method and the blue to the old method. Consequently, it can be seen in both plots that the estimation with the new method leads to a better performance of STELA that models the SRP acceleration. With better accuracy in the S/M estimation, the SRP perturbation is modelled more accurately, too, and the predicted curve of STELA comes closer to the observed data. All in all, in six out of ten cases, the new S/M estimation delivered a significantly better result compared to the algorithm already provided in OPERA. In all the other cases, there was no considerable difference between the propagation with the old and the new S/M estimation. It should be noted that the outcome also further depends on the quality of the first TLE in the time history, from where we start to propagate. Moreover, the simulation duration of the S/M estimation plays an important role, too, as can be seen when we compare Figure 10 with Figure 11 and Figure 12 with Figure 13. The longer the simulation duration the more TLEs are taken into account for the estimation as explained in subsection 5.1. The plots clearly show the deficits of the old S/M estimation while the new method demonstrates a better performance despite of the short simulation duration. Even though, a test with only ten samples is not sufficient to draw a statistical conclusion, the outcome of our test suggests that the S/M obtained from the old algorithm is less reliable.

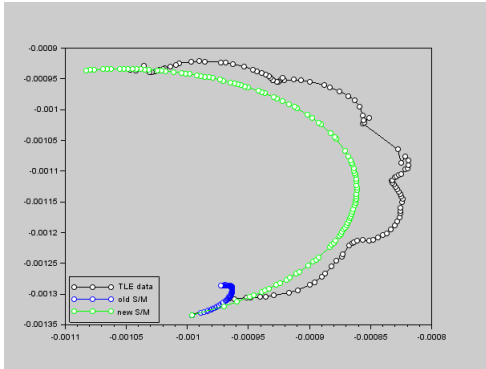


Figure 10: Evolution of \mathbf{e} of DFS Kopernikus 1 between 14/01/2016 and 29/06/2016 with a simulation duration of 13 days to compute the S/M estimation.

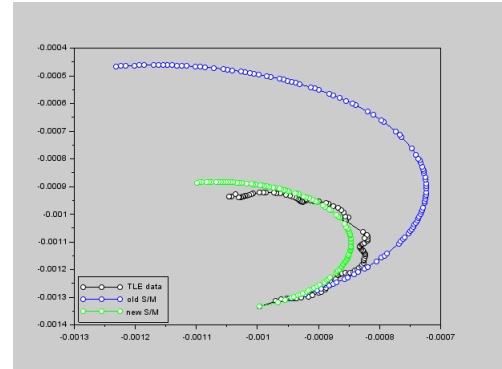


Figure 11: Evolution of \mathbf{e} of DFS Kopernikus 1 between 14/01/2016 and 29/06/2016 with a simulation duration of 30 days to compute the S/M estimation.

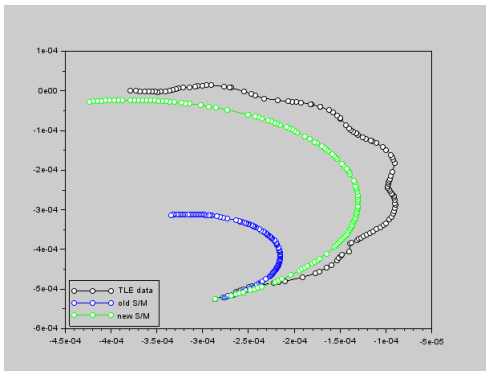


Figure 12: Evolution of \mathbf{e} of Telecom 2A between 14/01/2016 and 29/06/2016 with a simulation duration of 13 days.

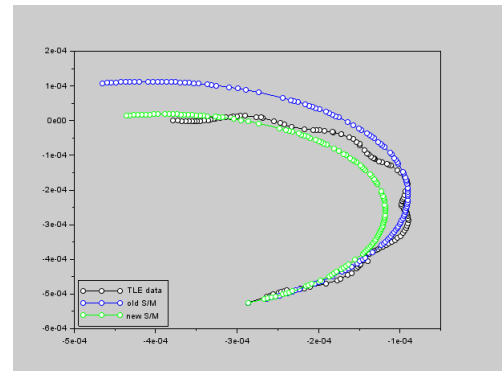


Figure 13: Evolution of \mathbf{e} of Telecom 2A between 14/01/2016 and 29/06/2016 with a simulation duration of 30 days.

6 Manoeuvre detection method

6.1 Classification of GEO objects

At the current moment, it is not yet possible to compute and identify the concrete manoeuvre performed by a S/C when analysing its TLE history in OPERA. However, it is possible to classify individual space objects into six categories:

- Liberation between stability points
- At a stable point (see subsection 3.5.1)
- On a drift orbit
- Still operational
- S/C made its last manoeuvre within the analysed time interval
- In LEOP

In addition to the status of a space object, OPERA returns the date of the starting point right after LEOP and the date of the last manoeuvre depending on the classification. The algorithm manages to classify the S/C into these categories by running through several tests that shall analyse the characteristics of the orbit and the behaviour of the S/C. A detailed description of these tests is given in the OPERA specification document by CNES.[15] The performance of classification algorithm was tested by Cid Borobia [18] using an ESA catalogue in order to compare the results. It has been found that the algorithm manages to correctly identify 94 % of 907 objects as operational and 97 % as non-operational S/Cs. Unfortunately, it has been noticed the specified categorisation achieve rather poor results as shown in Figure 14 and Figure 15. For the tests presented in these tables 400 objects were tested but it is unclear why the number of test objects has been reduced to 400 and under which criteria these objects were selected.

	In a drift orbit	between stability points	Object only under NSWE control	Object under WE control	object around eastern point	object around western point
Correct cases	405	9	247	29	64	25
Total cases	444	15	272	54	87	35
Percentage	91%	60%	91%	54%	74%	71%

Figure 14: Results of the object classification for 400 objects

	operational	not operational
cases correct	308	565
Total cases	326	581
Percentage	94%	97%

Figure 15: Results of the object identified as (non-) operational

Furthermore, the dates of the last manoeuvre that are detected by OPERA have not been verified. However, manoeuvre epochs are generally difficult to verify because the access to the manoeuvre history of the operator is needed in order to know when the manoeuvre was truly executed. Also, in our case, the test capacity is limited by the number of satellites where we have the operational manoeuvre history.

All in all, the manoeuvre analysis algorithm in OPERA for GEO satellites provides the basis in order to know if a satellite is operational or not. Only operational satellites are capable of performing manoeuvres in order to meet the requirements explained in subsubsection 3.4.1 throughout their mission phase. However, the algorithm is not capable of identifying individual manoeuvres. For this reason this project aims to extend the existing manoeuvre analysis in OPERA by providing a method how to detect in-plane manoeuvres from TLE data and gives an estimation of the size of the velocity increment ΔV required for the detected manoeuvre.

6.2 Overview of existing detection methods

Several methods already exist that aim to detect space events based on the analysis of the TLE history. A space event is defined as a sudden incident like a manoeuvre, an explosion, a collision, a fragmentation or a solar corona mass ejection that impacts the orbital state of a S/C.[19] Generally, there exists two principles of event detection methods:

- Comparison of the observed evolution with a reference model
- Application of robust statistics and harmonic analysis

In the first category, the reference model can either be a curve fit over the published orbital parameters or a propagated evolution using an accurate perturbation model. In both cases, the reference model gives a prediction of the state for an epoch t_n that is compared with the published observation from the TLEs at the same epoch. Such a procedure has been proposed by several researches with different approaches. Patera [20] proposed a detection method in which a moving curve fit technique is applied to the TLE data in order to filter noise and detect unexpected space events. In the algorithm of Li, Li, and Chen [19], the event detection relies on identifying abnormal segments of orbital parameters within the analysed time series. These abnormal segments mark the intervals at which the reference orbit produced by the SGP4 propagator deviates significantly from the observed ephemeris. Lemmens and Krag [21] propose to check the consistency of the TLEs in order to detect any anomalies due to a space event. According to the authors, the spatial difference between the propagated state and the following published state is small in case the S/C only encounters the natural perturbation forces modelled by the propagation model. In all those methods an outlier that violates the evolution of the reference model indicates the presence of a space event. Lemmens and Krag [21] also introduce another method that falls in the second category of the event detection principles. The TLE time series analysis uses robust statistics and harmonic analysis to identify unexpected variations in the evolution of the orbital parameters. For this purpose the algorithm searches for significant harmonics and estimates the noise of the time series while having low frequencies removed. The noise is then used to define a threshold that represents an expected range for the consecutive TLE. An event is indicated when the threshold is exceeded for a predefined amount of time.

All these proposed methods come with their advantages and disadvantages which are summarised in Table 5. It should be noted that these algorithms were tested by the authors and the advantages and drawbacks of the methods were derived from the presented results. According to these authors, one of the major problem is that most of these methods can only be applied to the LEO region. For example, Li, Li, and Chen states that the semi-major axis and the eccentricity have to be analysed because energy manoeuvres change the shape and size of the orbit. In contrast to this, inclination manoeuvres affect the orientation of the orbit in space that is manifests in an abrupt change of the inclination and the orbital node. Consequently, Li, Li, and Chen studies abnormal variation specifically in the evolution of the semi- major axis and the inclination. Nevertheless, from subsubsection 3.4.3 we recall, that energetic manoeuvres are rather directed tangentially and the change due to the manoeuvres in GEO is shown in the longitudinal drift and the eccentricity vector. That means for the detection of in- plane manoeuvres we are going to develop an algorithm that is based on the principle of comparing the observed data with the dynamic reference model STELA but instead we are analysing those orbital parameters which are more adequate for GEO. Moreover, after having studied the natural perturbation effects on

a GEO satellite, we are able to adapt the detection algorithm on the manoeuvre behaviour of those S/Cs encountering perturbations of different scales in comparison to LEO satellites.

	Pro	Cons
Space event detection method by Patera	<ul style="list-style-type: none"> • reliable in detecting abnormal events • not necessarily restricted to LEO • time/ computationally efficient 	<ul style="list-style-type: none"> • No differentiation between types of events • has only been proposed to detect energy changes
Manoeuvre detection method based on historical orbital data for LEO satellites by Li, Li, and Chen	<ul style="list-style-type: none"> • achieves high accuracy and credibility in tests 	<ul style="list-style-type: none"> • proposed for LEO • tuning of user specified parameters difficult • not able to detect manoeuvres if they are too close
TLE consistency check by Lemmens and Krag	<ul style="list-style-type: none"> • insensitive to natural events 	<ul style="list-style-type: none"> • proposed for LEO
TLE time series analysis by Lemmens and Krag	<ul style="list-style-type: none"> • can be applied to any orbit configuration • test show good performances 	<ul style="list-style-type: none"> • sensitive to sudden natural perturbations as for example to increase in solar activity

Table 5: Pro and cons of existing event detection methods

Furthermore, in our study, we assume that the events detected by the algorithm are only caused by manoeuvres. This assumption is only valid for those objects for which we know in advance that they have not exploded, collided and fragmented nor that a solar event has occurred within the analysed time interval. Eliminating all other causes that could lead to a space event leaves us with only one possibility: operational manoeuvres. For this reason, we will further refer to manoeuvre detection methods instead of event detection methods.

6.3 Principle of our method

The implementation of our method is based on a database of tracked space objects provided by United States Air Force that publishes the state of the S/Cs as a TLE catalogue. The TLEs are publicly available on www.space-track.org and taken as input parameters of our detection method. TLEs give a representation of the orbital state in the form of mean SGP4 elements defined with respect to the TEME frame. In order to work with the dynamical propagation model STELA, introduced in subsection 3.3, the elements need to be converted to mean STELA elements with respect to the integration frame CIRF. This transformation was explained in section 4.

As soon as the orbital parameters are converted in the correct mean element representation and in the appropriate reference frame, the plot of the parameter's evolution suggests a disruptive behaviour due to the presence of aberrant values that might result from the orbit determination in the TLE generation process. Before starting with the detection analysis, these aberrant values must be removed in order to avoid falsified results. In addition to filtering aberrant data point, we also need to guarantee that each data point is weighted equally. In some cases, the TLE catalogue gives two or more TLEs within one sidereal day while in other cases there is only one TLE per day. Therefore, we must iterate through the time series and remove all TLEs which are epoch- wise too close to each other.

Afterwards, the manoeuvre detection starts by studying the longitudinal evolution. Therefore, we are going to fit two curves over the longitudinal data. The first curve is derived from Equation 65 representing the physical longitudinal acceleration of a S/C. The second curve is obtained by a LS order-2 polynomial fit over the longitude data points. The intersections of the

LS parabolas are then considered as manoeuvre epoch. The accuracy of the estimated manoeuvre epoch depends on the disruptive evolution of the TLEs and the derivation between both curve fits. Consequently, it is convenient to label the estimated manoeuvre epoch with a confidential parameter that gives a time range around the estimation in which the true manoeuvre is expected.

The analysis is then continued by further studying the eccentricity vector evolution. Therefore, the interval characterized by the confidential parameter is forwarded to the eccentricity detection algorithm that shall identify the true manoeuvre epoch through the comparison with the propagated evolution by the dynamical model STELA. Afterwards, the required ΔV is computed derived from the change in the eccentricity vector. Because the sampling of the TLE data hinders us from recovering the actual number of burns and the size of each individual velocity change ΔV_i , we consider the manoeuvre as a single burn manoeuvre with the estimated ΔV as the effective velocity change due to all executed burns.

To conclude, the implementation can be summarised as follows:

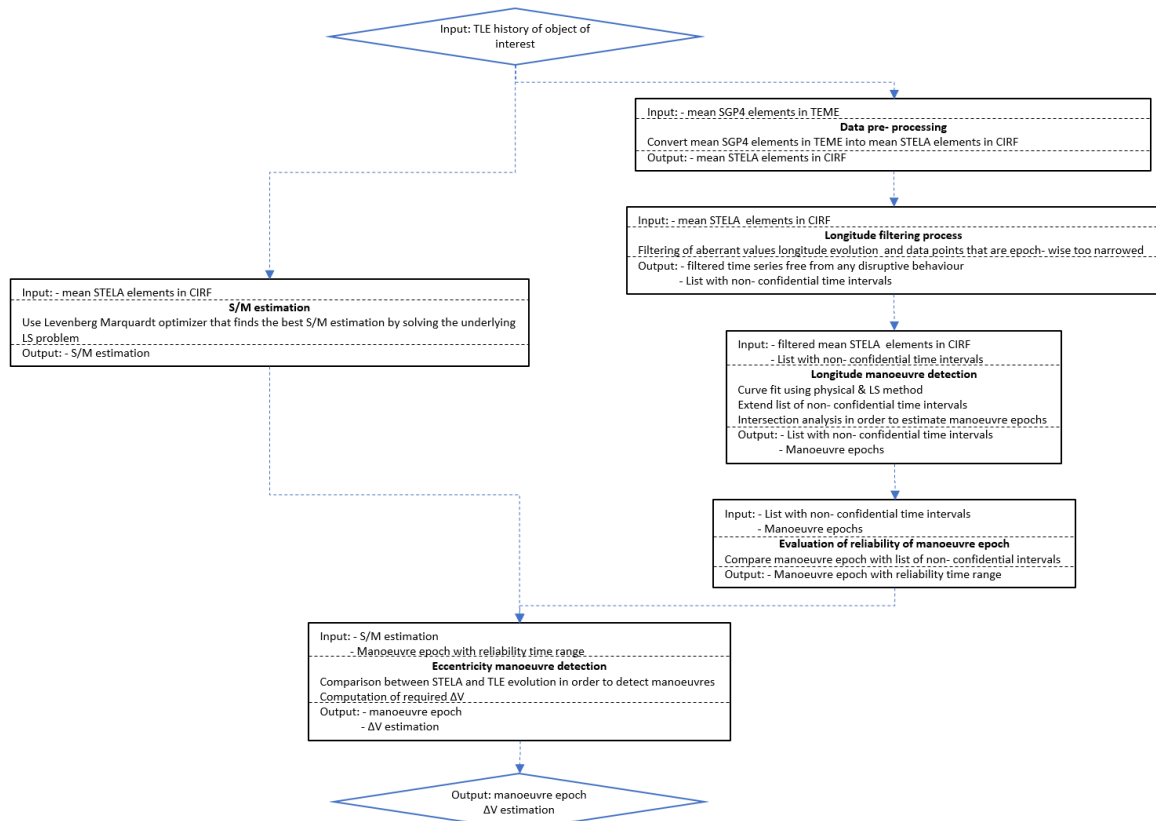


Figure 16: Overview of the proposed algorithm in order to detect and analyse in- plane manoeuvre. Note that each box does not represent the implementation of one single function but it is rather a collection of several functions in order to execute the instructions in the box.

6.3.1 Longitude analysis

In theory, the S/Cs remain fixed at the same sub-satellite point, if all perturbations have been neglected. However, in reality, the geo-gravitational potential is the main disturbing acceleration that lets this point drift along the equator.[22] Therefore, the operator needs to perform so-called station keeping manoeuvres that cause the S/C to maintain within a longitude window (the longitude deadband) and compensate the drift. As explained in subsection 3.5, the mean longitude motion describes a parabola function. Over time we retrieve a series of parabolas jointed by

cusps at the moments when a station keeping manoeuvre has been performed. Figure 17 shows an example for the Japanese satellite Himawari-8. In this case, the S/C accelerates towards the eastern stable point (75.1°E) and encounters a negative longitude acceleration. Consequently, the operator must fire a west burn as soon as the longitude motion violates the deadband.

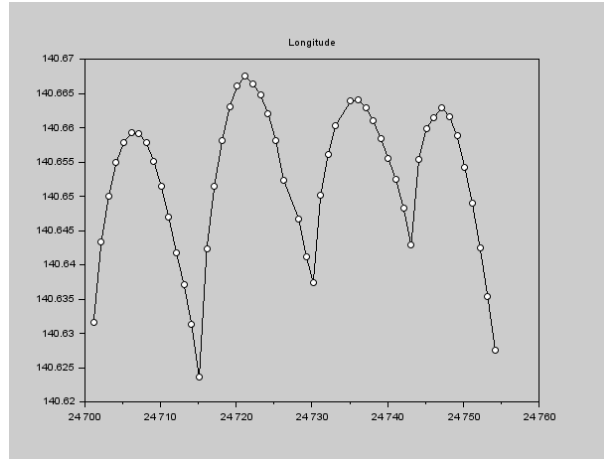


Figure 17: Longitude evolution [deg] of Himawari-8 between 17/08/2017 and 16/10/2017. The time is given in cjd. The mean longitude λ_m is estimated to be around 140.65 deg and the deadband half width $\delta\lambda$ is around 0.03 deg. The SK cycle starts at the west boundary of the deadband and the cusps indicate the presence of a manoeuvre to maintain the S/C around its mean longitude.

a) Filtering

Figure 17 is the plot of the S/C longitudes derived from its TLEs. Hereby, all aberrant TLEs and data points which are epoch-wise closer than 12h to each other have been removed after running through several filters. The objectives of the filters are:

- Removing multiple TLEs found within one revolution
- Removing large outliers which violate the deadband
- Removing outliers by correcting the longitude evolution

For the first objective, we loop through the entire time history and keep only one TLE per revolution. Due to previous tests, we have experienced that, in most cases, the first TLE is more reliable. Therefore, it had been decided to keep the first TLE in case multiple TLEs are present that are separated by less than 12h. Multiple longitudinal data within one day need to be removed since their presence could bias operations done on the data set as for example the computation of the mean longitude. Consequently, TLEs which are epoch-wisely too close to each other are removed through this method.

In the second step, big outliers shall be removed that violate the deadband. This filtering technique consists of two parts: In the first part, λ_m is set to the mean of the longitudes over the entire time history and the deadband half-width $\delta\lambda$ is initialized to 1 deg. All data points which violate this initial deadband are considered to be aberrant and are removed from the time history. In case more than 30% of the entire data set is removed, it is assumed that the object does not perform any station keeping manoeuvre. The selection of $\delta\lambda = 1$ deg as initial half-width is reasonable because the typical values range from 0.1 deg to 1 deg.[8]. In the second part, the current mean, minimal and maximal longitude over the entire time history are computed. $\delta\lambda$ is then defined in accordance to the current

minimum and maximum in the longitude evolution as followed:

$$\delta\lambda_{min} = \lambda_m - \lambda_{min} \quad (59)$$

$$\delta\lambda_{max} = \lambda_{max} - \lambda_m \quad (60)$$

$$\delta\lambda = \min(\delta\lambda_{min}, \delta\lambda_{max}) \quad (61)$$

As Equation 61 implies, the longitude extremum, that causes the larger half width dead-band size, is considered as an outlier and will be removed from the time history. Repeating this step, while constantly updating λ_m , λ_{min} and λ_{max} , will eventually lead to:

$$|\delta\lambda_{max} - \delta\lambda_{min}| \leq \epsilon \quad (62)$$

where ϵ is empirically set to 5×10^{-2} deg. Ideally, ϵ would have been zero, if λ_m had not been biased because of the sampling of the TLE data. Close to the vertex of a parabola, we have more longitude data than everywhere else. The reason for this is that at this point the longitude motion is decelerated due to presence of the nearest stable point that forces the S/C to accelerate towards the counter direction. That means, the longitude velocity is low at the vertex point which results in more TLE data close to this point than anywhere else. Accordingly, when the mean of the longitudes over the time history is computed, the result is slightly shifted towards the vertex points. In order to compensate the bias, ϵ has to be selected in such a way to be small enough to remove outliers but large enough to take the bias into account.

In the third step, we remove aberrant values from the time history while correcting the longitude evolution. In principle an outlier is a local extremum but an extremum does not necessarily have to be an outlier. Instead, an extremum can also be a vertex point or a cusp due to a manoeuvre. In the following, we will denote these kind of extrema as *true* extrema because these types do not disturb the behaviour of the parabola. Since the goal is to detect manoeuvres in the longitudinal evolution, we need to differentiate between these true extrema and the extrema due to outliers. Therefore, we iterate through the longitudes in the time history and extract all the local extrema. These extrema occur in so-called *bundles* which can vary in size as can be seen in Figure 18.

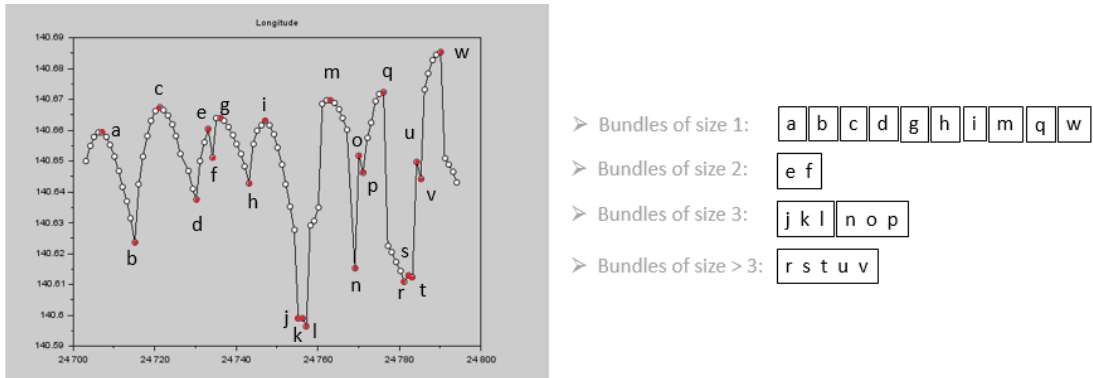


Figure 18: Longitude evolution [deg] of Himawari-8 between 17/08/2017 and 25/11/2017 after having removed multiple TLEs within one revolution and large outliers from the time history. The red dots mark the presence of a local extremum in the longitudinal evolution. Those extrema occur as bundles of different sizes: either they appear as an individual or as a sequence.

In contrast to bundles of size one whose extremum indeed indicate the presence of a true extremum, bundles of size $n > 1$ surely contain one or more outliers. Even though the latter disturb the parabolic trend of the longitudes, the trend can still be recovered, especially in the case of bundles of size two or three. In the following, these cases will be examined more in detailed:

i) Bundles with size two

As shown in Figure 19 there are only two scenarios in which these bundles can occur in the longitude evolution: either on the side of the falling or of the rising curve of the parabola. By knowing the underlying trend, we might be able to recognize the outlier in the bundle by comparing the values of the bundle with its neighbours. For example, knowing that the trend is falling, the maximum in the bundle cannot be higher than the left neighbour and the minimum cannot be lower than the right neighbour and vice versa in case of a rising trend. For this analysis, it should be guaranteed that the neighbours are not aberrant themselves. Nonetheless, we can be certain that this is not the case since each neighbour does not mark an extremum because otherwise the bundle would not be of size two but of size four. In case this analysis has not yet revealed the outlier in the bundle, we propagate the state with STELA starting from the epoch of the left neighbour towards both extrema epochs in the bundle. For the propagation, we need to estimate the S/M ratio of the S/C in order to achieve an accurate estimation for the state of the satellite. The estimation of S/M has been performed in section 5. STELA predicts the status of the S/C under consideration of the perturbation forces as presented in subsection 3.3 and the estimated longitudes are then compared with the observed data given by the TLEs.

$$\Delta E_1 = |\lambda_{prop,E_1} - \lambda_{E_1}| \quad (63)$$

$$\Delta E_2 = |\lambda_{prop,E_2} - \lambda_{E_2}| \quad (64)$$

ΔE_1 and ΔE_2 are the differences between the propagated longitude λ_{prop} retrieved from STELA and the longitude derived from the TLEs of the corresponding extrema E in the bundle. The extremum that generates the largest ΔE is considered as the outlier and will be removed from the time history. In case both extrema reveal a ΔE in the same range, both TLEs are considered as aberrant. In summary, this method will either remove both extrema in the bundle as outliers or only one of them and corrects the evolution of the parabola.

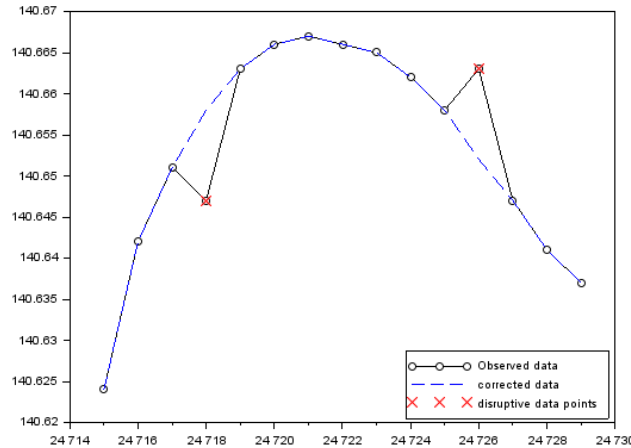


Figure 19: Example of a parabola with two bundles of size two. The outliers detected by the algorithm are marked in red. In the first case, STELA will recognize the underlying minimum as outlier while in the second case, the maximum directly reveals itself as aberrant because its longitude is larger than the one of the bundle's left neighbour.

ii) Bundles with size three

There are two scenarios that yield the case of having exactly three extrema in a row.

As can be seen in Figure 20 and Figure 21 the trend before and after the bundle is always reversed because the first and the last extremum are of the same type, either a maximum or minimum. Eventually, this leads to the conclusion that such bundles hide the presence of a true extremum. Knowing, that within the time interval of the bundle there must be a true extremum, will not help to eliminate the outlier but it will enable the recovery of the trend. For this purpose, one of the extrema needs to be removed from the time history and it was decided to always select the middle one. The reason for this is that we can be certain not to create a new bundle of size three as seen in Figure 21 but we make sure to have transformed the bundle into one of size one.

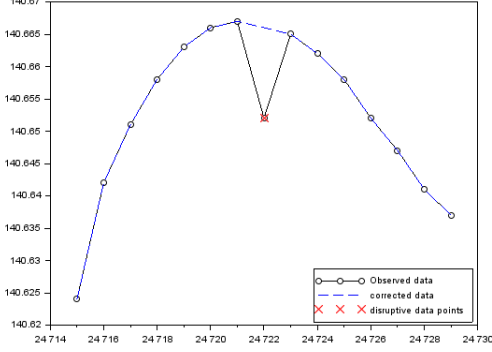


Figure 20: Example of a triple bundle at the vertex of the parabola.

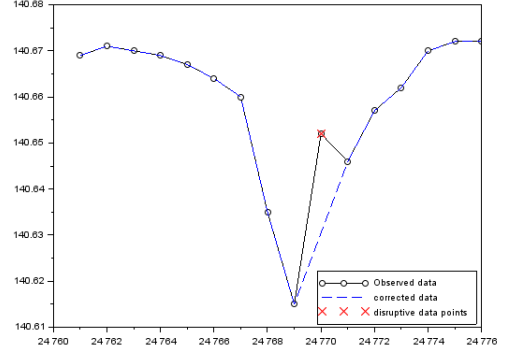


Figure 21: Example of a triple bundle that hides a true manoeuvre extremum.

Eventually, the data is nearly eligible for the fit of the parabolas. However, we need to keep in mind that the current longitudinal evolution is still disturbed by bundles of size larger than three. These kinds of bundles will be processed at a later stage in the algorithm. To recover the opening of the parabolas, it is necessary to compute the mean longitude over the entire time history. Moreover, it is significant to know which stable point is the closest one to the S/C to derive the direction towards it is accelerated. The direction of the opening of the parabola also gives the information about what type of in- plane SK manoeuvre is performed. An east SK manoeuvre is performed in case of a positive longitudinal acceleration and west SK burns are trusted to counteract a negative longitudinal acceleration. Accordingly, if we generally define the range of the longitudes to be between 0 deg and 360 deg, then we see that upwardly opened parabolas correspond to east manoeuvres and vice versa for the case of west manoeuvres.

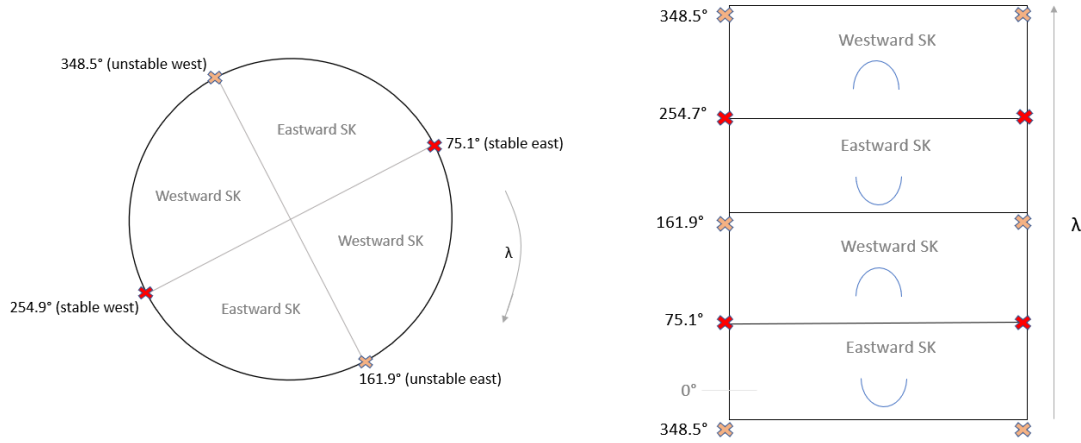


Figure 22: Relation between stability points and opening of parabola.

From the type of manoeuvre and the opening of the parabolas, we can derive if either the maxima or the minima in the longitude evolution mark the extrema related to the manoeuvre. In the case of Figure 17, the minima represents the *manoeuvre extrema* and accordingly, the maxima correspond to the vertex points of the parabolas, also denoted as *counter extrema*. At this point, we come back to the problem, that the longitudinal extrema may still be afflicted by bundles with more than three consecutive extrema. These bundles hinder the fit of the parabolas over the data points. However, analysing the concrete size and position in the longitude evolution of these bundles leads to the following possibilities in order to handle their disruptive behaviour:

- i In case the size of the time interval of the bundle is $< T$, where T is the mean duration between two manoeuvre extrema, and the bundle hides a true manoeuvre extremum, then the intersection between the flanking parabolas are capable of recovering the true extrema. In Figure 23, the flanking parabolas are the second and the third parabola in the illustration. Consequently, we remove the interval before we fit the parabolas over the longitudes. However, we will denote the recovered extremum by the intersection of the flanking parabolas (and the related manoeuvre epoch) as less reliable.
- ii In case the size of the time interval of the bundle is $< T$ but the bundle does not hide a true manoeuvre extremum, as presented in Figure 24, the action will be the same as in the first case. That means that we remove the disruptive interval of the bundle before the fit of the parabolas.
- iii This case creates the most problematic situation as seen in Figure 25. Due to the disruptive evolution of the TLEs, there is no way to analyse the manoeuvre history if the time interval is too long ($> T$).

As soon as there are no extrema in a row, which is equivalent to the presence of bundles only of size one throughout the entire evolution of the longitude, the filtering process is completed and the data is ready for the parabola fit.

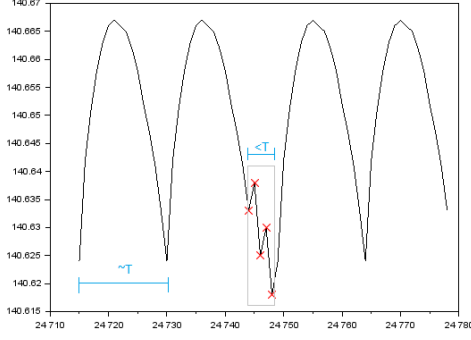


Figure 23: Example of a multi-extrema bundle that hides a true manoeuvre extremum

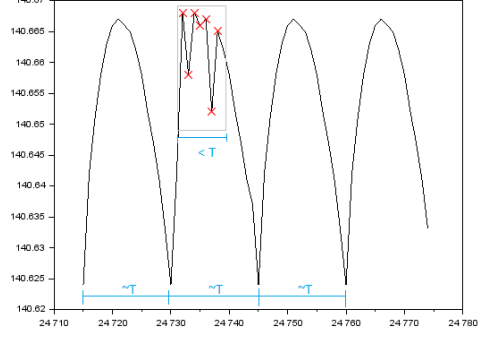


Figure 24: Example of a multi-extrema bundle that disrupts the evolution of a parabola

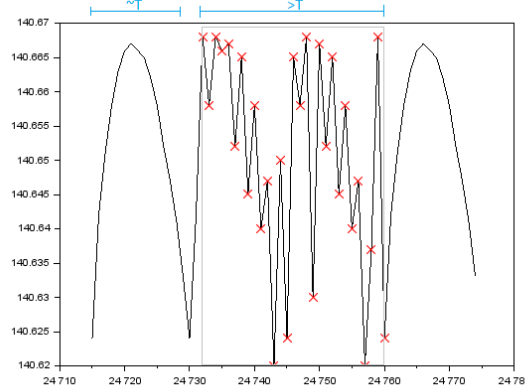


Figure 25: Example of a multi-extrema bundle that spans a time interval which is larger than T

b) Parabola fit

In the frame of this study, we have developed two techniques for the fit of a mathematical parabola equation over the observed data: the *physical* method and the method in which we consider the problem as a *Least square* problem. In both methods, a mathematical polynomial of second order shall be derived that gives the longitudinal motion over time. The S/C continues to follow the parabola as long as there is no further acceleration that gets the satellite off course such as a manoeuvre thrust. The derivation of the parabola equations using the two different techniques shall be presented in the following:

i) Physical method

As explained in subsection 3.5, one cannot consider Earth's gravitational attraction as symmetric and its mass concentrated in a point mass. Instead, the gravitational potential function given in Equation 38 is used to model the potential of the S/C encountering the gravity field of Earth. Also discussed in subsection 3.5 were the tesseral terms of the gravitational potential of Earth that cause an acceleration of the mean S/C longitude. The derivation of the acceleration is given in Appendix D for

which the gravitational potential has been analysed up to $l = 3$.

$$\ddot{\lambda} = -3n^2 \left[-6J_{22} \left(\frac{R_e}{a} \right)^2 \sin 2(\lambda - \lambda_{22}) + \frac{3}{2}J_{31} \left(\frac{R_e}{a} \right)^3 \sin(\lambda - \lambda_{31}) - 45J_{33} \left(\frac{R_e}{a} \right)^3 \sin 3(\lambda - \lambda_{33}) \right] \quad (65)$$

n denotes the mean motion of the S/C, λ its longitude and a its semi-major axis. R_e is the mean equatorial radius of the Earth and the J terms are the zonal harmonic coefficients of Earth's gravity field. Since the longitudinal deadband is usually very small, one considers the longitudinal acceleration as constant. Under this assumption, we can derive the solution for the longitude motion as follows:

$$\lambda = \lambda_0 \mp \dot{\lambda}_0 (t - t_0) \pm \frac{1}{2} \ddot{\lambda} (t - t_0)^2 \quad (66)$$

where 0 indicates the corresponding initial values at $t = t_0$:

$$\begin{aligned} \lambda_0 &= \lambda_m \pm \delta\lambda \\ \dot{\lambda}_0 &= 2\sqrt{|\ddot{\lambda}| \cdot \delta\lambda} \end{aligned} \quad (67)$$

As mentioned above, depending on the opening of the parabolas, the signs of Equation 66 change.[23] In order to have the parabola equation in the same format as for the LS fit, we are going to re-arrange Equation 66 into:

$$\lambda = a_p t^2 + b_p t + c_p \quad (68)$$

where:

$$a_p = \pm \frac{1}{2} \ddot{\lambda} \quad b_p = \mp (\dot{\lambda}_0 + \ddot{\lambda} \cdot t_0) \quad c_p = \pm \frac{1}{2} \ddot{\lambda} \cdot t_0^2 \pm \dot{\lambda}_0 \cdot t_0 + \lambda_0$$

Here, the subscript p marks the coefficients derived with the physical method of fitting the parabolas. Note, that the upper signs are valid for a positive longitude acceleration. In case the S/C performs west station keeping manoeuvres, the signs below are valid.

The physical fit sets up an equation that does not take into account all parameters that could potentially affect the longitudinal behaviour of the S/C. It only considers to a certain degree the harmonics of Earth's potential and neglects for example the S/C's eccentricity and inclination. The fitted parabolas are then just representing a model which eventually reaches its limit in terms of accuracy. In turn, that will create an impact on the estimation of the manoeuvre epoch since the deviation of the eccentricity and inclination vector has been neglected. In addition, it might occur, that some days before an EW manoeuvre, a NS manoeuvre has been performed that may disturb the longitudinal motion. For these reasons, it is reasonable to fit the data using a least square method, which is presented in the next step.

ii) Least square method

The idea of least square is a common approach in regression analysis and statistics to determine the line of best fit over a given data set. The underlying principle in our case aims to generate a curve of second degree that is laid over the data in such a way that the sum of the squared residuals resulting from the differences between the observed and the fitted data points on the curve are minimized. Adapted to our problem, the goal is to find a, b and c such that Π is minimized:

$$\Pi = \sum_{n=1}^m [y_n - (aT_n^2 + bT_n + c)]^2 \quad (69)$$

where m is the number of TLE data within the time history and y_n denotes the observed longitude derived from the TLEs. For the sake of a better readability, we have introduced the variable T_n that is defined as:

$$T_n := (t_n - t_0)$$

The underlying linear equation system is given as:

$$\begin{bmatrix} \sum 1 & \sum T_n & \sum T_n^2 \\ \sum T_n & \sum T_n^2 & \sum T_n^3 \\ \sum T_n^2 & \sum T_n^3 & \sum T_n^4 \end{bmatrix} \begin{pmatrix} a \\ b \\ c \end{pmatrix} = \begin{pmatrix} \sum y_n \\ \sum T_n y_n \\ \sum T_n^2 y_n \end{pmatrix} \quad (70)$$

where \sum actually means the sum through all the TLE data $\sum_{n=0}^m$. In order to have the parabola equation in the same format as for the LS fit, we are going to re-arrange the resulting parabola equation of Equation 70 into:

$$\lambda = a_{LS}t^2 + b_{LS}t + c_{LS} \quad (71)$$

where:

$$a_{LS} = a \quad b_{LS} = b - 2c \cdot t_0 \quad c_{LS} = a \cdot t_0^2 - b \cdot t_0 + c$$

The subscript LS marks the coefficients of the parabola equation derived with the least square method.

We have seen that there exist two ways to fit the parabolas over the given dataset but both methods have their advantages and drawbacks. Figure 17 suggests that even after the filtering process the data still seem to be defected, not due to outliers but rather to the accuracy of orbital determination procedure that has generated the TLEs. Generally, if the observed data can be trusted, the LS method delivers good approximations of the true longitudinal behaviour of the S/C. On the other hand, the physical approach uses a model to fit the data points and may be able to correct the drawbacks of the LS approach. Depending on the accuracy of the model, the LS and the physical approach should yield the same result. We see in Figure 27 that the fitted parabolas are very close to each other, if the observation data are good enough, resulting in the conclusion that the model derived in the physical method is indeed sufficiently accurate. Consequently, in case the fitted parabolas of both methods are not aligned, it indicates that the TLE data are less confidential in order to return a good estimation of the true manoeuvre date. Hence, we cannot rely on the result given with the LS method and it drives the need to introduce a so-called “confidential parameter”. As indicated previously, this parameter denotes all manoeuvre estimations as “not reliable” if the fitted parabola from the physical method deviates too much from the LS parabola.

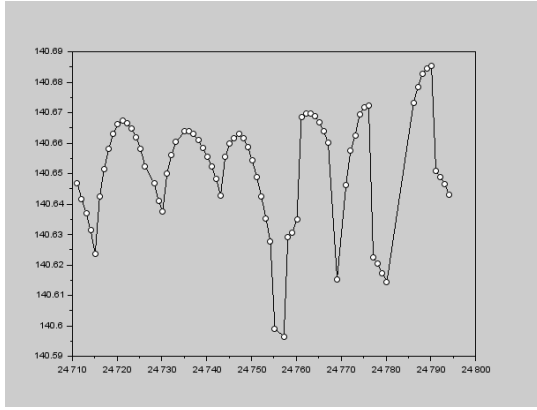


Figure 26: Longitude evolution [deg] of Himawari-8 between 27/08/2017 and 25/11/2017 after all extrema bundles with size larger than one have been removed. However, the last three parabolas indicate the presence of non reliable TLEs.

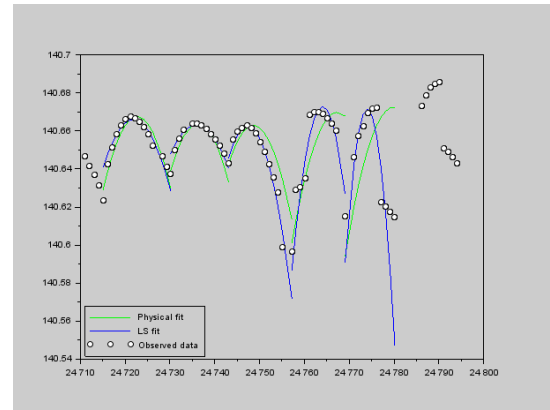


Figure 27: Parabola fit with physical and LS method over the data of Himawari-8. The first three parabolas are well fitted but due to the following non-reliable data, the fit with LS and the physical approach deviate a lot.

c) Confidential parameter

Throughout the manoeuvre analysis we have extracted all time intervals which are assumed to be too disruptive to estimate the manoeuvre epoch accurately. The confidential parameter shall mark the estimated manoeuvre epoch as less reliable in case the parabola interval contains aberrant time series. There are two occasions within the algorithm at which the program evaluate the reliability of the data: during the search for aberrant parabolas, during the process when bundles of multiple extrema are removed and during the comparison of the physical and LS fit.

Concerning the first occasion, we will search for aberrant parabolas that do not originate from the SK cycle but from the orbit determination explained in subsubsection 3.4.2. Aberrant parabola may occur in the longitudinal evolution if the orbital determination process reveals some unstable results. An indication of the presence of aberrant parabolas is when the related counter extrema or the manoeuvre extrema are in the wrong half deadband with respect to the mean longitude over the entire time history. In this case, the corresponding time interval of the aberrant parabola is stored for the later use among all the other non- confidential intervals. For the second occasion, we will not only remove the interval of the disruptive bundle from the time interval but we will store the time interval of the corresponding parabola with some margin in order to recognize the detected manoeuvre epochs related to this parabola. The size of the margin includes half of the interval of the parabolas before and after the erroneous parabola. Since the data of this parabola is regarded as not confidential, the resulting intersection analysis can only be trusted together with a larger error interval. For the third occasion, when the fitted parabola of the two methods are compared to each other, we must define a threshold to be able to consider the parabolas' evolution as similar or displaced. For this reason, we sum up the absolute distances between both fits and considered the currently analysed parabola interval as not confidential, if the error is larger than a certain sensitivity threshold. This threshold is the mean error between the minimal and the maximal error that occurs within the time series. In summary, the reliability relies on those three parameters:

- *absolute distance*: The deviation between both fits at epoch i .
- *error*: The sum of all the absolute distances over one parabola interval.
- *sensitivity*: The mean value of the errors that occurs throughout the entire time history:

$$\text{sensitivity} = \min(\text{allErrors}) + \frac{\max(\text{allErrors}) - \min(\text{allErrors})}{2} \quad (72)$$

where *allErrors* is the collection of all error values within the entire time history.

In the end, each manoeuvre epoch carries an attribute "reliable" in the form of a boolean that is by default set to true. As a result, all the detected manoeuvre epochs which lie within the non confidential time interval are treated as less reliable and the attribute is then set to false. Consequently, the manoeuvre epochs not affected by any abnormal TLE data reveal an accuracy within the range of one to two days. In contrast to this, detected manoeuvres within the non confidential time interval usually deviate by several days from the true manoeuvre epochs.

d) Intersection analysis

As previously explained, the parabola fits using LS are preferred over the physical method and are therefore considered for the intersection analysis. The underlying principle is that the intersection between two consecutive parabolas reveals the estimated manoeuvre epoch. Assuming that the equations of parabola 1 and 2 are:

$$\lambda_1 = a_1 t^2 + b_1 t + c_1 \quad \lambda_2 = a_2 t^2 + b_2 t + c_2$$

then the zeros of the intersection equation are at:

$$t_{1,2} = \frac{-(b_1 - b_2) \pm \sqrt{(b_1 - b_2)^2 - 4(a_1 - a_2)(c_1 - c_2)}}{2(a_1 - a_2)} \quad (73)$$

In order to be considered as manoeuvre epoch, the related longitudes at t_1 or t_2 must lay within the longitude deadband. Finally, it is checked if the estimated manoeuvre epoch is contained within the non-confidential time intervals so that each estimation can be assigned to the correct confidential parameter.

6.3.2 Eccentricity analysis

In subsubsection 3.4.3 we have seen that a single longitude manoeuvre cannot change the longitude without affecting the behaviour of the eccentricity vector. Consequently, it is advisable to couple the manoeuvre detection with the longitudinal and the eccentricity vector evolution. In our method, the longitude manoeuvre detection is performed over the entire time interval of interest. The longitude algorithm returns a list of epochs of the estimated manoeuvres within this interval. The eccentricity manoeuvre detection is then only applied to each individual manoeuvre epoch in the list instead of to the entire time interval of interest. That says, that in the eccentricity analysis, a small interval around the manoeuvre epoch is studied to ensure that the smaller interval only contains one manoeuvre. In the following, we will refer to these small intervals as manoeuvre intervals.

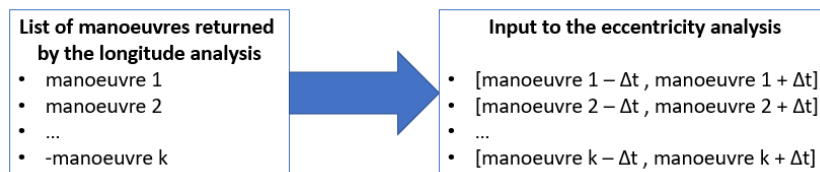


Figure 28: Interface between the longitudinal and the eccentricity analysis

In principle, the algorithm can be generalised and applied to the entire time history. This enables the detection of manoeuvres which correct the eccentricity and are decoupled from the longitude strategy. However, this generalisation will increase the risk of false positive manoeuvre detection as we are going to discuss in subsection 7.2.2. Therefore, in the current implementation, the eccentricity analysis is only applied to the manoeuvre intervals.

The principle of the eccentricity analysis relies on the prediction of the S/C's behaviour computed by STELA. Because \mathbf{e} is mainly influenced by the effect of the SRP, the STELA propagation needs to take into account a well estimated value of the S/M that induces this perturbing effect. The algorithm will compare the observed \mathbf{e} with the propagated state and assumes that a manoeuvre was performed in case the difference exceeds a certain noise threshold value. This threshold was empirically set to 1.3×10^{-5} and has been chosen by comparing the STELA propagation with the eccentricity vector evolution of several non- operational satellites which do not perform any manoeuvres. These analyses have shown that the difference between the prediction of the dynamical and the observed data does not overstep a value of 1.3×10^{-5} . However, this threshold depends on the performance of the model and on the estimated S/M. The less accurate the propagation with the dynamical model, the higher the threshold becomes and the larger the risk of false negative manoeuvre detections. Instead one must find a compromise in setting the threshold in such a way that the propagation error is subtracted while remaining large outliers that are due to a manoeuvre.

In the following, we are going to focus on the implementation of the manoeuvre detection using the evolution of \mathbf{e} and derive a method of how to estimate $\Delta \mathbf{V}$ required for this manoeuvre.

Similar to the algorithm for the S/M estimation and the longitude detection, the orbital parameters must be converted from mean SGP4 elements to mean STELA elements according to the algorithm described in section 4. Afterwards, aberrant data points and TLEs which are epoch wise too close to each other are filtered following the filtering techniques presented in the longitude analysis. For the propagation process, the state of the S/C at each TLE epoch is propagated to the consecutive TLE epoch as illustrated in Figure 29.

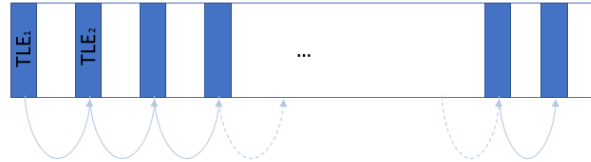


Figure 29: STELA propagation starting from each TLE epoch to the consecutive epoch

Only at the first TLE epoch, the observed eccentricity vector is equal to the propagated state because a preceding TLE does not exist. Otherwise, at each epoch, the difference between the observation and the prediction by STELA can be computed. The dynamical model predicts the state of the S/C under the assumption that it only encounters natural perturbation forces. In reality, the S/C might perform manoeuvres which perturb the orbital state in addition but the thrusts are not taken into account by the dynamical model. Consequently, any large deviations between the dynamical model and the observed evolution indicates the presence of a manoeuvre. For our analyses, \mathbf{e} is split into its x - and y - component so that the differences are defined as:

$$\mathbf{diff}_x = \left| \begin{pmatrix} e_{x,TLE_1} \\ e_{x,TLE_2} \\ \vdots \\ e_{x,TLE_m} \end{pmatrix} - \begin{pmatrix} e_{x,STELA_1} \\ e_{x,STELA_2} \\ \vdots \\ e_{x,STELA_m} \end{pmatrix} \right| \quad \mathbf{diff}_y = \left| \begin{pmatrix} e_{y,TLE_1} \\ e_{y,TLE_2} \\ \vdots \\ e_{y,TLE_m} \end{pmatrix} - \begin{pmatrix} e_{y,STELA_1} \\ e_{y,STELA_2} \\ \vdots \\ e_{y,STELA_m} \end{pmatrix} \right| \quad (74)$$

Afterwards, we iterate through \mathbf{diff}_x and \mathbf{diff}_y and set all the entries to zero, in case the value lies below the threshold of 1.3×10^{-5} . The resulting sets of \mathbf{diff}_x and \mathbf{diff}_y pertains one of the following possibilities:

- a) \mathbf{diff}_x and \mathbf{diff}_y contain one maximum each at the same epoch. Consequently, the manoeuvre epoch is evident and can be recovered from the TLEs.
- b) \mathbf{diff}_x and \mathbf{diff}_y contain one maximum each but not at the same epoch. Since the size of the interval is selected in such a way that it only contains one single manoeuvre, it is assumed that the combination of both maxima indicate the manoeuvre. In this case, the manoeuvre epoch is also assumed to be evident and can be recovered from the TLEs.
- c) \mathbf{diff}_x and \mathbf{diff}_y contain several maxima and for this reason the true manoeuvre epoch is not evident.
- d) \mathbf{diff}_x and \mathbf{diff}_y do not contain any maxima. This suggest that either there is no manoeuvre in the time interval that can be recovered or the manoeuvre is too small and therefore hidden in the TLE noise or the manoeuvre is composed of several burns that effectively eliminate the change of the eccentricity vector, as discussed in subsubsection 3.4.3. Either way, in all three cases the manoeuvre epoch is not evident.
- e) Only one set (either \mathbf{diff}_x or \mathbf{diff}_y) contains a maximum but the other does not. In this case, it is assumed that the recovered maximum corresponds to a manoeuvre and the related manoeuvre epoch is evident and can be recovered from the TLEs.

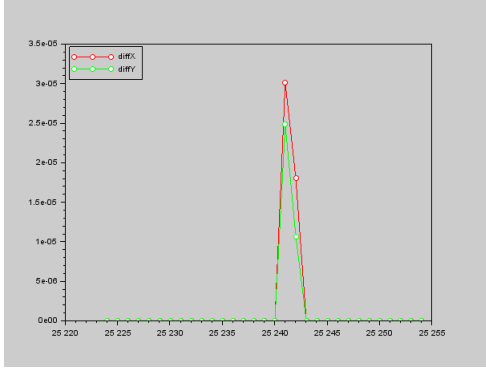


Figure 30: Difference in the x - and y -component of \mathbf{e} between TLE observation and STELA propagation at each epoch in the manoeuvre interval. This shows an example of case a) where the peak of both components are located at the same epoch.

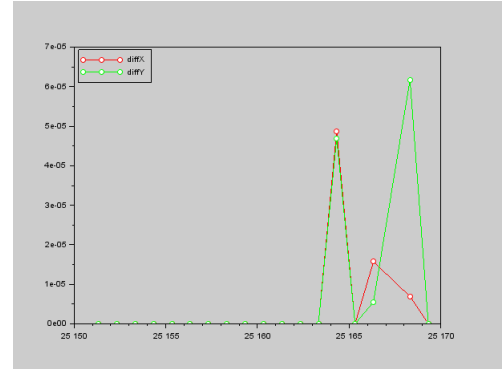


Figure 31: Difference in the x - and y -component of \mathbf{e} between TLE observation and STELA propagation at each epoch in the manoeuvre interval. This shows an example of case c) where the manoeuvre cannot be recovered.

Accordingly, the velocity increment $\Delta \mathbf{V}$ caused by the manoeuvre can only be computed if the manoeuvre epoch is evident as it is the case for a), b) and e). Following these cases, the manoeuvre day must lay between the first TLE where the deviation between STELA and observation exceeds the threshold and the previous epoch. Nevertheless, the algorithm is not capable of recovering the number of thrust nor the size of each individual $\Delta \mathbf{V}_i$ or the exact thrust time of each burn $t_{b,i}$. Instead, it is considered that the manoeuvre is performed as a single burn manoeuvre at epoch t_b and $\Delta \mathbf{V}$ is then derived from $\Delta \mathbf{e}$ that is defined as:

$$\Delta \mathbf{e}(\zeta) = \begin{bmatrix} e_{x,TLE}(\zeta) - e_{x,STELA}(\zeta) \\ e_{y,TLE}(\zeta) - e_{y,STELA}(\zeta) \end{bmatrix} \quad (75)$$

ζ marks the epoch at which the entries of \mathbf{diff}_x and \mathbf{diff}_y fall below the threshold value again, after the evolutions of the TLEs and STELA have deviated due to the manoeuvre. In contrast to the previously propagated values, $e_{x,STELA}(\zeta)$ and $e_{y,STELA}(\zeta)$ are not obtained by propagating the orbital state from epoch $\zeta - 1$ but from epoch α , where the entries of \mathbf{diff}_x and \mathbf{diff}_y were still below the threshold value before the manoeuvre took place. Hence, epoch

α indicates the moment at which the manoeuvre has not yet affected the orbital state but is manifests one epoch later at $\alpha + 1$. In the Figure 30, epoch α corresponds to 25 240.02 cjd and epoch ζ to 25 243.017 cjd. Consequently, the right hand side of Equation 75 shows the difference of the observed eccentricity vector after the manoeuvre and the expected value if the manoeuvre had not been performed. Furthermore, we assume that the operator has intended to perform a pure longitudinal manoeuvre which means that the radial and orthogonal component of $\Delta \mathbf{V}$ are zero. Therefore, we leave off the subscript "t" in the velocity change while keeping in mind that $\Delta V = \Delta V_t$. From subsubsection 3.4.3, we know that the eccentricity change due to a tangential is given by Equation 46:

$$\Delta e = \frac{2\Delta V}{V} \begin{bmatrix} \cos s_b \\ \sin s_b \end{bmatrix} \quad (25)$$

ΔV results from the change of the numerical eccentricity:

$$\Delta V = \frac{|\Delta e| V}{2} \quad (76)$$

where V is the velocity of the unperturbed geostationary S/C. Applying Equation 76, Equation 25 can be rewritten as:

$$\Delta e = |\Delta e| \begin{bmatrix} \cos s_b \\ \sin s_b \end{bmatrix} \quad (77)$$

Due to the symmetry of the trigonometrical functions sine and cosine, it is not sufficient to only solve the equation in one component but the solution s_b must solve both terms in Equation 77. The resulting s_b gives the angular position of the S/C on the orbital plane at the moment of the burn with respect to the \mathbf{X} - axis (see Appendix A). That means, that s_b represents the fraction of the day at which the burn was fired. The exact manoeuvre hour of the day t_b is then retrieved by means of any reference point on the orbit where the epoch and the sidereal angle are known. We denote the epoch of this reference point as t_{ref} and its sidereal angle as s_{ref} . t_b is then given by:

$$t_b = t_{ref} - \frac{12}{\pi} \cdot (s_{ref} - s_b) \quad (78)$$

The day of the manoeuvre lies between the TLE epoch where \mathbf{diff}_X and \mathbf{diff}_Y have not exceed the threshold and its consecutive epoch day.

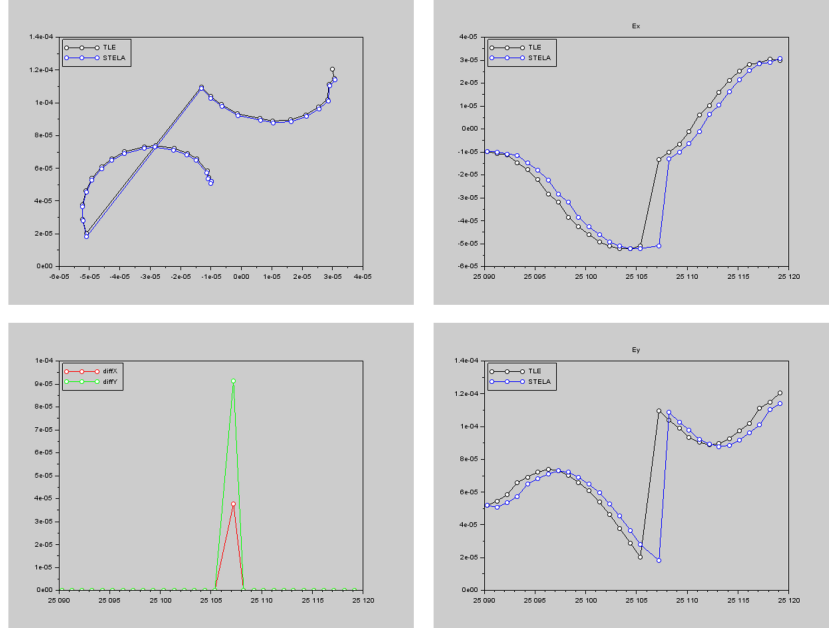


Figure 32: Eccentricity analysis on Meteosat 9 between 11/09/2018 and 11/10/2018 showing the evolution of the eccentricity vector according to the TLE data and STELA propagation (upper left), the evolution of the eccentricity vector split in x - and y - components (right side) and the deviation between observed data and STELA prediction (bottom left).

7 Results

7.1 Tests

As it was indicated in subsection 6.1, the test capacity is limited by the number of objects of which the manoeuvre history is known. In our study, we have the manoeuvre history of 31 satellites in GEO but in some case the manoeuvres are only given for a finite time interval and not for the entire time of life of the S/C. The list of these reference objects was generated by the Space Debris modelling and risk assessment office of CNES. Furthermore, in the frame of this project, we have not managed to automatize the testing process. Within the short period of time, we were forced to test our implementation by the "brute force" method which means that the objects and time interval to analyse were loaded manually to the longitude algorithm and the returned list of estimated manoeuvres was then compared with the operational table by hand. The same problem applies for the eccentricity, where each individual manoeuvre interval was forwarded to the consecutive analysis in order to estimate the hour of the day at which the manoeuvre was performed. In the following we present the results from the analysis of the longitude and eccentricity vector. In the first part, five objects were randomly selected out of the list of the 31 reference objects and a total number of 143 manoeuvres has been studied in order to test the performance of the longitude analysis. Also, in the second part, where the day fraction of the manoeuvre epoch is estimated by analysing the eccentricity vector, the results are compared with the manoeuvre epochs of the operator history. Since the interface between the longitude and eccentricity analysis shown in Figure 28 is not yet implemented, we have to manually set the input of the eccentricity algorithm. Consequently, we only managed to test the performance of this part of the detection method by means of three objects with a total number of manoeuvres of 29. In the following the results of both analysis are presented more in detail.

7.1.1 Longitude analysis

The performance of the longitude analysis is evaluated by comparing the estimated manoeuvre epoch with the operational history. In case the true epoch manoeuvre lies within the manoeuvre interval around the estimated epoch, the estimation is considered to be correct. The size of the manoeuvre interval depends on the confidential parameter which is set according to the reliability of the TLE data as explained in subsubsection 6.3.1. In the end, the performance of the manoeuvre detection depends on the relative number classified in the following cases with respect to the total amount of tests. In the scope of our project, we managed to test this part of the manoeuvre detection algorithm by means of five reference objects with a total number of 143 manoeuvres performed by these S/Cs. The test satellites which have been randomly selected were:

- Inmarsat 3 F3 - GB (24674)
- Inmarsat 3 F5 - GB (25153)
- Telecom 2C - France (23730)
- Inmarsat 3 F1 - GB (23839)
- Telecom 2D - France (24209)

Table 6 shows the results of all tested satellites. As previously mentioned, the total number of true manoeuvres given by the operator histories was 143 which is the sum of FN, P and NP. Our algorithm managed to detect 109 manoeuvres in total but this number includes not only the positive detections but represents the sum of FP, P and NP. It follows that our algorithm was able to (nearly) correctly detect 67.83 % of the true manoeuvres. Table 6 also represents the results of each individual test satellite. It shows that Telecom 2C accounts for more than 70 % of the total FN detections. If this satellite is excluded from the results the positive and nearly positive rate rises from 67.83 % to 85.06 %. In subsubsection 7.2.1, we discuss the reasons for the large FN rate of Telecom 2C and propose a method of how the algorithm can be improved.

	FP	FN	P	NP	\sum manoeuvres	\sum detected
Inmarsat 3 F3	-	3	18	-	21	18
Inmarsat 3 F5	-	1	23	-	24	23
Telecom 2C	5	33	19	4	56	28
Inmarsat 3 F1	-	6	17	1	24	18
Telecom 2D	7	3	11	4	18	22
All	12	46	88	9	143	109

Table 6: Results of the longitude detection analysis of each individual test satellite with the number of detections which has been categorized as false positive (FP), false negative (FN), positive (P), and nearly positive (NP). The latter classifies all the positive detection where the estimation deviated too much from the true manoeuvre epoch. In the tests, this deviation went up to eight days

7.1.2 Eccentricity analysis

The performance of the eccentricity analysis is evaluated by comparing the estimated manoeuvre epoch with the operational history. In case the estimation deviates by less than one hour from the true manoeuvre hour, the prediction is seen as a positive detection, a deviation between one and two hours is considered as nearly positive and everything else counts as a negative detection. The performance is only analysed with respect to the estimated hour of manoeuvre because the objective was to estimate the sidereal angle at the time of the manoeuvre. Nevertheless, the algorithm also returns the manoeuvre day, however, the estimated day systematically lays one to two days behind the true manoeuvre day.

Within the short period of time, we only managed to test three objects which has been selected randomly from the list of reference objects. The test satellites were:

- Inmarsat 3 F3 - GB (24674)
- Inmarsat 3 F1 - GB (23839)
- Meteosat 9 - EUMETSAT (28912)

	Good estimations	Fair estimations	Bad estimations	Total manoeuvres
Inmarsat 3 F3	8	1	5	14
Inmarsat 3 F1	4	5	2	11
Meteosat 9	3	-	1	4
All	15	6	8	29

Table 7: Results of the eccentricity detection analysis of each individual test satellite

Table 7 shows the number of detections which has been classified as good, fair and bad estimation compared to the operator history. Consequently, if the good and fair estimations are summarized, the eccentricity analysis method has been able to (nearly) correctly estimate the manoeuvre hour with a rate of 72.41 %. In subsubsection 7.2.2, we discuss how this rate can be improved and the reasons for bad estimations with the eccentricity detection method.

7.2 Discussion

In the following, we are going to discuss the results presented in subsection 7.1. Generally, bad tests results might either derive from a bad performance of the detection algorithm or from the test principle itself. In both detection methods, in the longitude and eccentricity analysis, the number of test cases was very small. In order to better evaluate the performance of the detection algorithm the number of tests must increase significantly in order to draw any statistical conclusions. We will still try to analysis the performances from the test results and discuss probable limits of both detection methods. Since the longitude and eccentricity vector analysis have been separately tested from each other, the discussion of the results is split in two parts.

7.2.1 Longitude analysis

Before the results presented in subsubsection 7.1.1 are analysed, it is necessary to differentiate between the number of manoeuvres within the time interval of interest and within the interval of recoverable manoeuvres. In all of our tests within the longitude analysis we have noticed that in some cases the first two manoeuvres are systematically not detected in the time interval of interests. The underlying reason for this is that we have intentionally implemented the algorithm in such a way that a manoeuvre is only identified if two parabolas intersect with each other. For the first parabola there exists no preceding parabola and, hence, there is no intersection nor can the manoeuvre be detected. The case that the first two manoeuvres are not detected appears when the time interval is set in a way that the first TLE epoch already presents a manoeuvre epoch according to the operator history. That means that the related parabola truly hides two manoeuvres that cannot be recovered because it is the first parabola in the time interval. Since we have systematically excluded the first and the last parabola from the fitting process, the interval of possible detection is smaller than the time interval of interest. Consequently, the worst case scenario is that four manoeuvres are excluded from the fitting interval, as shown in Figure 33. When the performance of the algorithm is evaluated, the manoeuvres related to the first parabola should not be taken into account and the same applies for the last parabola. For this reason, we should not analyse the number of detections compared to the true number of manoeuvres within the time interval of interests but rather within the interval in which the parabola curve fitting is performed. Moreover, this also means that the longitudinal manoeuvre detection requires as an input the evolution of more than three parabolas in order to make at least one manoeuvre estimation.

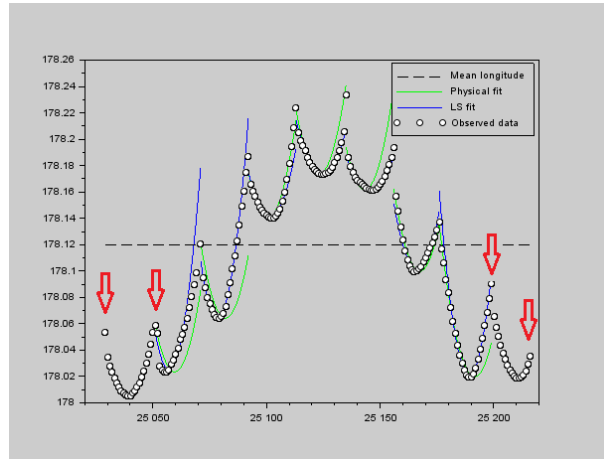


Figure 33: Longitude evolution [deg] of Inmarsat-3 F3 between 11/07/2018 and 16/01/2019. The first two and last two manoeuvres (indicated by red arrows) are not detected because they correspond two the first and last parabola in the time interval that are excluded from the parabola fitting process.

It can be further seen in Figure 33 that the algorithm encounters a problem when the confidential parameter is set depending on the occurrence of aberrant parabolas. In subsubsection 6.3.1, we said that a parabola is considered as aberrant if either the counter extrema or the manoeuvre extrema are in the wrong half deadband with respect to the mean longitude over the entire time history. In the case shown in Figure 33 the parabolas do not lie in the same longitude band and consequently, the computed longitudinal mean, illustrated by the dashed line, does not represent the mean longitude of each individual parabola. Even though the manoeuvre detection does not suffer under this circumstance, the algorithm classifies each parabola interval as non confidential and the related manoeuvre epochs as less reliable even though the estimation is good.

More important, one of the major drawbacks of our method is that we are not capable of recovering each individual burn throughout a manoeuvre phase due to the sampling of the observation. If a manoeuvre is composed of more than one burn the combined effect can only recovered from the longitudinal evolution. That means for the following manoeuvre history given in Table 8 the algorithm only gives one estimation for the manoeuvre epochs.

Epoch (cal)	Epoch (cjd)
2018-08-22T17:03:30.000	25070.71076
2018-08-22T17:15:00.000	25070.71875
2018-08-22T17:56:09.999	25070.74734

Table 8: Extraction from manoeuvre history of Inmarsat-3 F3. The algorithm gives only one manoeuvre estimation for all three burns, that is on 20/08/2020. The estimation counts as a positive detection because the manoeuvre interval contains the true epoch.

The results presented in Table 6 combine the amount of burns over one day to one manoeuvre. That means that the given number of total true manoeuvres represents the number of manoeuvres that might be composed of several burn. Hence, this issue does not explain the large rate of FN detections. However, it follows, that the algorithm reaches its limit in case the station keeping cycle is very short. Even though satellite operators usually schedule the cycles in such a way that the time between two manoeuvres is as long as possible to save fuel, there exists S/Cs which perform manoeuvres nearly on the daily base. Inmarsat-4 F1 is an example that manoeuvres at the latest every two days. Even though we can recover some parabolic shapes as shown in Figure 35, the cusps only present a fraction of the total amount of manoeuvres. Also in this case, the problem is related to the data sampling. If there is only one TLE per day, the amount of data is not enough to recover short station keeping cycles. We encountered this problem with one of our test satellite (Telecom 2C) which revealed a large FN detection rate.

The algorithm rather considers the extrema, that are in fact due to manoeuvres, as bundles of multiple aberrant values and removes them from the time interval. The filtering of those manoeuvres results in a large number of false negative detections. The detection might be improved by a combination of the proposed method and the TLE time series analysis presented by Lemmens and Krag. For objects with a short station keeping cycle this approach will likely recover the false negative detections of our method. In fact, the manoeuvre detection of LEO objects that already exists in OPERA relies on the analysis of the harmonics but with orbital parameters that are better suited for the region of LEO.

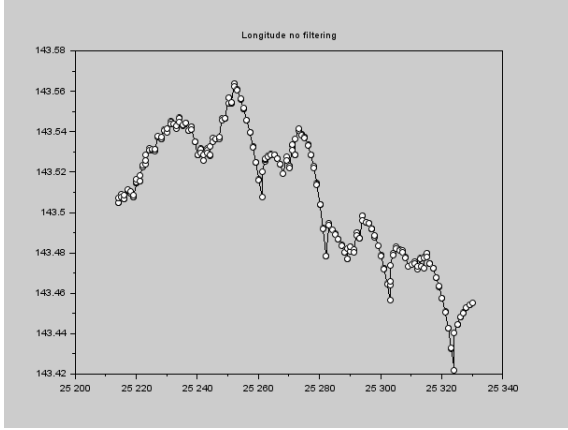


Figure 34: Longitude evolution [deg] of Inmarsat-4 F1 between 12/01/2019 and 09/05/2019 without any filters.

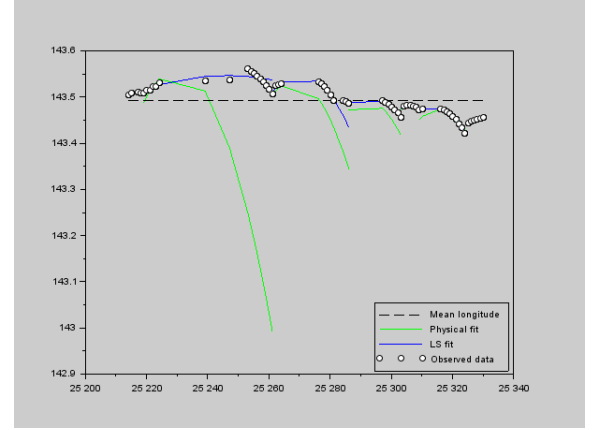


Figure 35: Longitude evolution [deg] of Inmarsat-4 F1 between 12/01/2019 and 09/05/2019 with fitted parabolas.

Another possible explanation for the high rate of FN might be due to the lack of information in the operator history concerning the type of the manoeuvre. In some cases, the operator history does not specify if the recorded manoeuvre is an in- plane or an out- of- plane manoeuvre. Since it is assumed that this manoeuvre is a longitude manoeuvre, the missed detection is taken into account in the statistic as FN detection even though the true manoeuvre could have been rather an inclination change.

In contrast to this, the algorithm is prone to FP detections in case the longitude evolution contains aberrant parabolas. Aberrant parabolas do not originate from the station keeping cycle but from the orbit determination. As explained in subsubsection 3.4.2, the TLEs are generated by a numerical fit of the orbit over discrete measurements of the S/C's state over a certain time interval. Aberrant parabola may occur in the longitudinal evolution if the orbital determination process reveals some unstable results. In order to suppress further FP detections, one must find a way to filter these aberrant parabolas while not increasing the risk of removing true manoeuvres and thereby increasing the number of FN detections. The function adjusting the confidential parameter with respect to possible aberrant parabolas presents a way how these parabolas can be detected. However, we have seen previously the problems of this method and therefore, it has been decided to leave the aberrant parabolas in the longitude evolution and take the risk of FP manoeuvres.

7.2.2 Eccentricity analysis

The results presented in Table 7 show the estimation of manoeuvres where the manoeuvre epoch could be recovered depending on the deviation between TLE and STELA evolution. In contrast to this, case c) that has been presented in subsubsection 6.3.2 occurs when this deviation reveals several maxima in the time interval. Figure 36 and Figure 37 show this scenario that occurred for Inmarsat-3 F1. The interval reveals more than one maximum in the x - and y - component of the eccentricity vector of the deviation. Only from the operator history we know that the

first maximum starting at epoch 25 520 cjd is due to the manoeuvre while the second maximum starting from 25 523 cjd shows an aberrant behaviour in the TLE data that deviates from the expected behaviour predicted by STELA. One would think that aberrant values have been already removed after the filtering process of in the longitude analysis. However, there the data were filtered in order to recover the longitudinal trend. It might happen that the algorithm does not recognize a data point as aberrant because its longitudinal value is still compliant with the trend of the parabola. Hence, the value does not represent a problem in the longitudinal analysis because it does not create an extremum in the longitude evolution but it might show its aberrant characteristic in the eccentricity analysis as in the example of Inmarsat-3 F1.

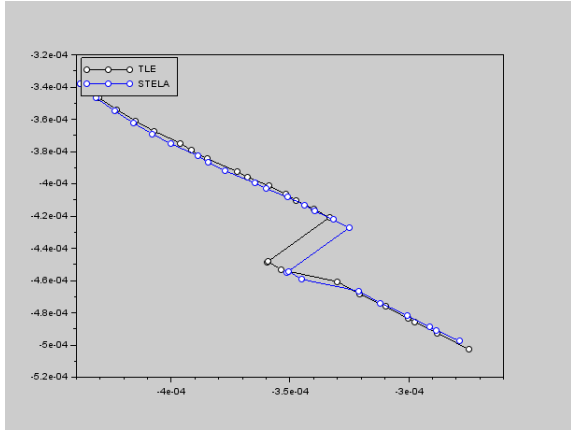


Figure 36: Eccentricity vector evolution of Inmarsat-3 F1 between 31/10/2019 and 27/11/2019.

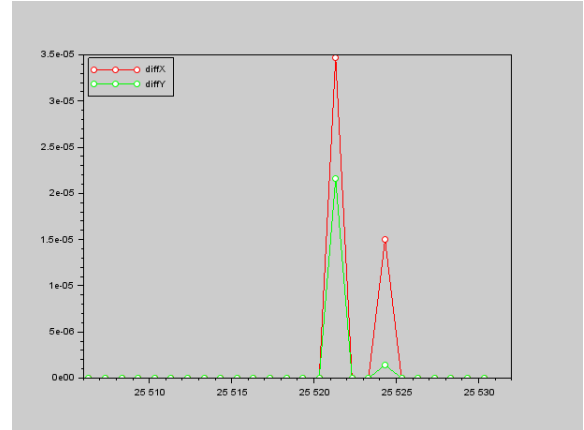


Figure 37: Difference in both components of e between TLE and STELA evolution at each epoch in the manoeuvre interval.

With respect to the recoverable manoeuvres, Table 7 shows that in eight out of 29 cases, the estimation of the manoeuvre hour was poor. A possible explanation for that might be the width of the peaks of the deviation between TLE evolution and STELA propagation ($diff_x$ and $diff_y$) shown in Figure 30. One might think that a manoeuvre changes instantaneously the behaviour of the orbital parameter and consequently, the peaks of $diff_x$ and $diff_y$ must be very narrowed. In theory, the deviation between the true state of the S/C and the prediction by the dynamical model is non-zero only at the instance of the manoeuvre. However, TLEs do not necessarily represent the true state of the satellite, especially in case a manoeuvre was performed. When a satellite has manoeuvred, the orbit determination process might generate the following TLE from an interval that takes into account measurements before and after this manoeuvre. This scenario is shown in Figure 38 where the manoeuvre is illustrated by the jump of the blue line representing the true behaviour of the orbit. The width of the peak consequently depends on the duration it takes until the determined orbit recovers from the manoeuvre. This point is reached when the interval of the orbit determination only takes into account measurements of the orbital state after the manoeuvre took place. Figure 39 illustrates the effect of the TLE generation on the manoeuvre detection algorithm. The red circle represent the epochs at which the deviation between TLE and STELA lies below the threshold before and after the manoeuvre, respectively. Hence, the distance between the circles represent the width of the peak shown in Figure 30. That says the larger the width, the more time has passed since the true manoeuvre epoch. This has an effect on the computation of the Δe that is defined as the change in the eccentricity vector due to a single burn manoeuvre. If a long time passes since the manoeuvring, Δe will additionally be affected by the natural perturbations. Hence, recovering the effect only due to the manoeuvre is impossible and the resulting estimation of the manoeuvre hour is less accurate.

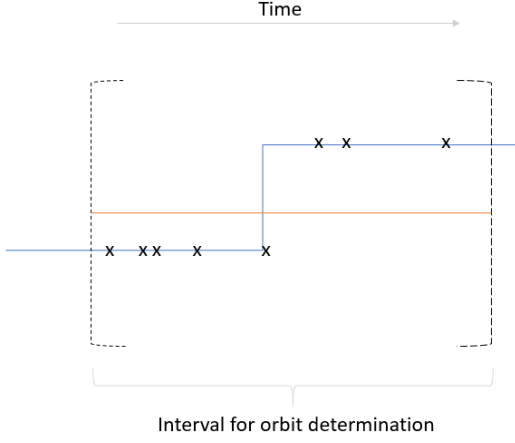


Figure 38: Illustration of orbit determination process showing the true behaviour of the orbit (blue), the measurements that have been taken into account to determine the orbit (black) and the determined orbit itself (red).

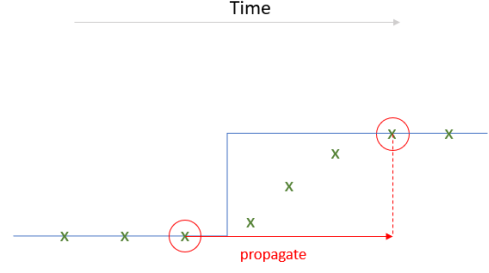


Figure 39: Effect of manoeuvre on the nature of the TLEs showing the true behaviour of the orbit (blue) and the evolution of the TLEs (green). The red circles mark the width of the peak seen in Figure 30.

Furthermore, a large peak width generates another problem related to the performance of STELA. The longer it takes for the TLE evolution to recover from the manoeuvre, the longer we need to propagate with STELA right from the point before the deviation between observation and predicted state has exceeded the threshold to the point where the deviation falls below the threshold again. STELA, however, encounters a problem when the integration step size is too large. In general, the propagation duration must be a multiple of the integration step size. In our case, the integration step size has to be set equal to the propagation duration in order to guarantee that we propagate to the exact same epoch as given in the TLE to compare the observation with the predicted state according to the dynamical propagation model. It seems that when the integration step size is too large, the propagation with STELA escapes. This case is shown in Figure 40 where the propagated evolution of the inclination is seen starting from a set of random mean elements and epoch 20000. The blue curve is the normal propagation with a constant integration step size of 86 400 s. The circled black points show the propagation to some specified epochs in this time history starting from the very first epoch. Thereby, the integration step size is set equal to the propagation duration and is adjusted for the propagation to the next specified epoch. Consequently, the integration step size grows and it can be seen that in the evolution of the specified propagation starts to deviate from the normal propagation.

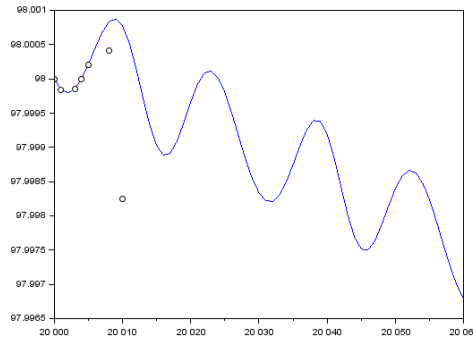


Figure 40: Propagated inclination evolution [deg] with an integration step size set to 86 400 s (blue) compared to the evolution of a propagation with growing step size over time (black).

It follows that we need to reduce the integration step size in order to have a better prediction of the state in case the propagation duration is long. Therefore, it had been decided to round each TLE with an accuracy of one hour so that the integration step size can be constantly set to one hour (3600 s). Thereby, we ensure that the propagation duration is a multiple of the integration step and that the observation is compared with the expected value at the same epoch. With these adaptations, we could correct two bad estimations in Table 7 to good estimations and the rate of (nearly) correctly estimated manoeuvre hours was improved from 72.41 % to 79.31 %. Another error source that can result in a bad estimation is the assumption of having a single burn manoeuvre. For the computation of the sidereal angle we have assumed that the manoeuvre consist of only one burn and we have used the equation of the eccentricity vector change due to a single burn manoeuvre of subsection 3.4.3. However, the results show that in most cases, the manoeuvre hour could still be recovered.

Even though the focus of the eccentricity analysis is set on the estimation of the time during the day where the manoeuvre was performed, the analysis still returns an estimation of the manoeuvre day. In our tests, this estimation was always one to two days later from the true manoeuvre day according to operator history. The reason for this is the orbit determination and the generation of the TLE history. When a S/C performs a manoeuvre the change of its orbital state is not immediately manifested in the TLE history. Consequently, the deviation between the observed orbital state and the prediction does not exceed the threshold at the moment when the S/C executes the manoeuvre but after a certain time shift. Consequently, the estimation of the manoeuvre day is systematically shifted in time.

8 Conclusion

In the scope of this work project, we developed two techniques to detect in- plane manoeuvres. The first method focuses on the longitude evolution and aims to recover the SK cycle by fitting the parabolic evolution of the longitude data and analysing their intersection. The tests have shown that the method reaches its limit if the SK cycle is too short or if the sampling of the TLEs is too small to optimally fit the parabola evolution. The method might be extended by the analysis of the harmonics in the time series as it is presented by Lemmens and Krag [21] in order to reduce the number of FN detection due to short manoeuvre cycles. The second method analyses the behaviour of the eccentricity vector and compares the observed evolution with the expected state predicted by the dynamical propagation model STELA. A manoeuvre is detected as soon as the derivation between both evolution exceeds a certain threshold value. The performance of this detection method strongly depends on the performance of the dynamic model because it models the natural perturbation forces acting on the S/C. We learnt that among those forces, the SRP is the dominant term that affects the evolution of the eccentricity vector. The perturbing effect, however, is induced by the effective S/M of the S/C, hence, the modelling of the SRP acceleration depends on an accurate estimation of the S/M. This estimation is retrieved by solving the LS problem using the Levenberg Marquardt optimizer.

All the tests, in order to evaluate the performance of the S/M estimation, the longitude detection and eccentricity detection algorithm, were suffering from a small number of test cases. Consequently, the test capacity must increase that might reveal better results than the one we gained in this project. Moreover, in the frame of this study we have only focused on the detection of in- plane manoeuvres. However, we expect to be able to detect out- of- plane manoeuvres, too, by a method similar to the eccentricity analysis but with the inclination vector as parameter to study. For now, our algorithm was only implemented in scilab because it provides through its plotting tools an optimal environment to firstly develop the algorithm before it is implemented to OPERA. In OPERA, the manoeuvre detection is not yet optimized for GEO satellites and we hope to extend the software by our proposed detection algorithm in the future. The ability to recover the manoeuvre history of satellites is important to analyse the life time of a satellite. In particular, it is of huge interest to know if a satellite has already reached its end of life and if its last manoeuvre has been performed in accordance to the IADC mitigation guidelines.

References

- [1] A. Sinha, *SpaceX crew dragon: A new era in space exploration*, <https://indianexpress.com/article/explained/spacexs-crew-dragon-nasa-astronauts-international-space-station-6436442/>, [Online; accessed 01-June-2020], 1 June 2020.
- [2] H. Krag, *The space debris environment*, 13 May 2019.
- [3] J. N. Pelton *et al.*, *Space debris and other threats from outer space*. Springer, 2013.
- [4] I.-A. S. D. C. Committee *et al.*, “Iadc space debris mitigation guidelines,” URL: http://www.iadc-online.org/Documents/Docu/IADC_Mitigation_Guidelines_Rev1_Sep07.pdf, 2007.
- [5] D. A. Vallado, *Fundamentals of astrodynamics and applications*. Springer Science & Business Media, 2001, vol. 12.
- [6] D. A. Vallado and P. J. Cefola, “Two-line element sets—practice and use,” in *63rd International Astronautical Congress, Naples, Italy*, 2012.
- [7] A. Celletti, *Orbit determination*, 21 April 2011.
- [8] E. M. Soop, *Handbook of geostationary orbits*. Springer Science & Business Media, 1994, vol. 3.
- [9] H. D. Curtis, *Orbital mechanics for engineering students*. Butterworth-Heinemann, 2013.
- [10] G. J. Der and R. Danchick, “Conversion of osculating orbital elements to mean orbital elements,” 1996.
- [11] D. Vuckovic, P. Rajkovic, D. Jankovic, and O. Pavic, “Guidelines for satellite tracking,” *Satellite Communications*, p. 283, 2010.
- [12] F. R. Hoots, P. W. Schumacher Jr, and R. A. Glover, “History of analytical orbit modeling in the us space surveillance system,” *Journal of Guidance, Control, and Dynamics*, vol. 27, no. 2, pp. 174–185, 2004.
- [13] “User’s guide stela,” *CNES*, vol. 2.5, 2013.
- [14] F. R. Hoots, R. L. Roehrich, and T. Kelso, “Spacetrack report no. 3,” *Project Spacetrack Reports, Office of Astrodynamics, Aerospace Defense Center, ADC/DO6, Peterson AFB, CO*, vol. 80914, p. 14, 1980.
- [15] Goester, Jean-François, *Specifications techniques du produit logiciel opera*, 2020.
- [16] Wikipedia contributors, *Levenberg–marquardt algorithm — Wikipedia, the free encyclopedia*, [Online; accessed 10-August-2020], 2020. [Online]. Available: https://en.wikipedia.org/w/index.php?title=Levenberg%E2%80%93Marquardt_algorithm&oldid=971681349.
- [17] D. A. Vallado, P. Crawford, R. Hujsak, and T. Kelso, “Revisiting spacetrack report# 3: Rev 1,” in *AIAA/AAS Astrodynamics Specialist Conference and Exhibit*, 2006.
- [18] E. Cid Borobia, “Detection of manoeuvres in space debris catalogue,” 2014.
- [19] T. Li, K. Li, and L. Chen, “New manoeuvre detection method based on historical orbital data for low earth orbit satellites,” *Advances in Space Research*, vol. 62, no. 3, pp. 554–567, 2018.
- [20] R. P. Patera, “Space event detection method,” *Journal of Spacecraft and Rockets*, vol. 45, no. 3, pp. 554–559, 2008.
- [21] S. Lemmens and H. Krag, “Two-line-elements-based maneuver detection methods for satellites in low earth orbit,” *Journal of Guidance, Control, and Dynamics*, vol. 37, no. 3, pp. 860–868, 2014.
- [22] P. Berlin, *The geostationary applications satellite*, 2. Cambridge University Press, 1988.
- [23] S. Borissov, Y. Wu, and D. Mortari, “East–west geo satellite station-keeping with degraded thruster response,” *Aerospace*, vol. 2, no. 4, pp. 581–601, 2015.

- [24] M. Soffel, S. A. Klioner, G. Petit, P. Wolf, S. Kopeikin, P. Bretagnon, V. Brumberg, N. Capitaine, T. Damour, T. Fukushima, *et al.*, “The iau 2000 resolutions for astrometry, celestial mechanics, and metrology in the relativistic framework: Explanatory supplement,” *The Astronomical Journal*, vol. 126, no. 6, p. 2687, 2003.

A Frames definition

Frame	Acronym	Definition	Comments
International Celestial Reference	ICRF	<ul style="list-style-type: none"> • O: Barycentre of Solar System • Z: points towards ICRS pole which is consistent to Earth's mean pole at J2000 with an offset by less than 20 milliarcseconds • X: close to the dynamical equinox at J2000 but with an offset of around 78 milliarcseconds • X-Y plane consistent with mean equator at J2000. The effects of Earth's precession and nutation have been averaged out 	<p>Quasi inertial system</p> <p>Ideal reference frame derived from the coordinates of extragalactic radio sources observed with VLBI</p>
Barycentric Celestial Reference	BCRF	<ul style="list-style-type: none"> • O: Barycentre of Solar System <p>No fixed definition of orientation of spatial axis</p>	<p>Metric tensor specified according to IAU 2000 B1.3 [24]</p> <p>In praxis: BCRF is orientated according to ICRF</p>
Geocentric Celestial Reference	GCRF	<ul style="list-style-type: none"> • O: Earth's centre of mass <p>No fixed definition of orientation of spatial axis</p>	<p>Metric tensor specified according to IAU 2000 B1.3 [24]</p> <p>GCRS is defined such that it is kinematically non- rotating with respect to BCRF</p> <p>In praxis: GCRF is orientated according to BCRF (ICRF)</p>
Celestial Intermediate Reference	CIRF	<ul style="list-style-type: none"> • O: Earth's centre of mass • Z: points towards CIP • X: points towards CEO • Y: orthogonal trihedron 	<p>Considers the precession-nutation model</p> <p>Used as integration frame in STELA</p>
Earth mean equator and equinox at epoch J2000	EME2000	<ul style="list-style-type: none"> • O: Earth's centre of mass • Z: orthogonal to the plane defined by the mean equator at J2000.0 • X: mean equinox at J2000.0 epoch • Y: orthogonal trihedron 	<p>Quasi initial frame at fixed epoch</p> <p>The mean equator of date (MOD) frame is defined in the same way but also takes Earth's precession into account</p> <p>The true equator of date (TOD) frame is defined in the same way but refers to the true equator and true equinox and accounts for precession/nutation effects</p>
True Equa- tor Mean Equinox	TEME	<ul style="list-style-type: none"> • O: Earth's centre of mass • Z: points towards true rotation axis of current epoch • X: points towards mean vernal equinox of current epoch • Y: orthogonal trihedron 	<p>Frame in which the TLE are displayed</p>

B Radial manoeuvre

When a single radial manoeuvre is performed the conditions of Equation 8 to Equation 13 simplify to:

$$0 = \Delta r = -A \left(\frac{2}{3} \Delta D + \Delta e_x \cos s_b + \Delta e_y \sin s_b \right) \quad (79)$$

$$0 = \Delta \lambda = \Delta \lambda_0 + \Delta D (s_b - s_0) + 2\Delta e_x \sin s_b - 2\Delta e_y \cos s_b \quad (80)$$

$$\Delta V_r = V (\Delta e_x \sin s_b - \Delta e_y \cos s_b) \quad (81)$$

$$0 = \Delta V_t = V (\Delta D + 2\Delta e_x \cos s_b + 2\Delta e_y \sin s_b) \quad (82)$$

The solution of this equation system is given by

$$\Delta \lambda_0 = -\frac{2\Delta V_r}{V} \quad (83)$$

$$\Delta D = 0 \quad (84)$$

$$\Delta \bar{e} = \bar{e}_{new} - \bar{e}_{old} = \frac{\Delta V_r}{V} \begin{bmatrix} \sin s_b \\ -\cos s_b \end{bmatrix} \quad (85)$$

The longitude drift rate D and the semi major axis a are not affected by this type of manoeuvre but the change of the eccentricity vector points orthogonal to \bar{r} and is only half as large as in the case of a tangential thrust. Therefore, radial thrust are not as efficient as longitude manoeuvres.

C Solar and Lunar attraction

The gravitational attraction of the Moon and the Sun considered as point masses due to their far distance also influence the orbit and behaviour of the S/C. Denoting the potentials of Earth, Sun and Moon respectively as μ , μ_1 and μ_2 and their position with respect to the satellite as $-\mathbf{r}$, $\mathbf{r}_1 - \mathbf{r}$ and $\mathbf{r}_2 - \mathbf{r}$, the combined gravitational attraction of these three bodies acting on the S/C is:

$$\left(\frac{d^2 \mathbf{r}}{dt^2} \right)_{3rdBody} = -\frac{\mu}{r^3} \mathbf{r} + \sum_{k=1}^2 \frac{\mu_k}{|\mathbf{r}_k - \mathbf{r}|^3} (\mathbf{r}_k - \mathbf{r}) \quad (86)$$

where \mathbf{r}_1 and \mathbf{r}_2 represents the solar and lunar position relative to Earth. Since the Earth also moves under the influence of Sun and Moon, its acceleration is given by:

$$\left(\frac{d^2 \mathbf{r}}{dt^2} \right)_{Earth} = \sum_{k=1}^2 \frac{\mu_k}{r_k^3} \mathbf{r}_k \quad (87)$$

Subtracting Equation 87 from Equation 86 results in the acceleration and subsequent motion of the S/C in the Mean Equatorial Geocentric system (Appendix A):

$$\frac{d^2 \mathbf{r}}{dt^2} = -\frac{\mu}{r^3} \mathbf{r} + \sum_{k=1}^2 \mu_k \left[\frac{\mathbf{r}_k - \mathbf{r}}{|\mathbf{r}_k - \mathbf{r}|^3} - \frac{\mathbf{r}_k}{r_k^3} \right] \quad (88)$$

The distances r_k to Sun and to Moon are much greater than the distance to Earth r which means that the term in the brackets of Equation 88 nearly gets cancelled out. The remain effect can be better visualised by linearly expanding in r/r_k of the term inside the brackets:

$$\frac{d^2 \mathbf{r}}{dt^2} \approx -\frac{\mu}{r^3} \mathbf{r} + \sum_{k=1}^2 \frac{\mu_k}{r_k^3} \left[\frac{3}{r_k^2} (\mathbf{r}_k \cdot \mathbf{r}) \mathbf{r}_k - \mathbf{r} \right] \quad (89)$$

We see that the term on the right side within the brackets causes a negative and radial acceleration acting on the S/C towards Earth. In contrast to this, the first term in the bracket represents the acceleration towards the Sun or Moon but the sign depends on the position of all three bodies (S/C, Earth and body k). The term becomes positive during half of a day when the S/C is on the same side of the Earth as body k . However, on the other half of the day the signs of \mathbf{r} and \mathbf{r}_k differ and the term becomes negative. From the physical aspect the S/C is more attracted by the Moon and the Sun when the S/C is on the same side as them with respect to Earth and with growing distance during the other half of the day the attraction becomes less. Moreover, one would expect that the Sun create the more dominant perturbation effect due to its higher gravity potential compared to the Moon. However, its distance compensates the attraction so that the net resulting perturbation from Moon is even twice as strong as from the Sun in the Mean Equatorial Geocentric system:

$$\frac{3\mu_1 r}{r_1^3} = 0.5 \times 10^{-5} \text{ m s}^{-2} \quad \frac{3\mu_2 r}{r_2^3} = 1.1 \times 10^{-5} \text{ m s}^{-2}$$

Splitting the acceleration effect into an in- plane and out- of- plane component helps to analyse the effect on the orbital parameter. The out- of- plane component will influence the long-term evolution of the inclination vector

drift. The radial component however attains a maximum twice per day when the S/C is on the same or opposite side as body k with respect to Earth. Hence, the perturbing in plane acceleration is the strongest when the three bodies are positioned in a line and the smallest when the angle between body k , Earth and S/C is a right angle. Furthermore, this perturbing effect on the S/C's orbit results in a maximum twice per month, when Earth, Sun and Moon are closely aligned. This might remind us of an similar effect we know from the behaviour of the ocean during spring and neap tides. Hence, the constellation of the tidal bodies affects the shape of the orbit and the parameters a , λ and e . For the evolution of a and λ , it results in some short-term variations of about a few kilometres and milli degrees. With respect to the eccentricity vector, its mean motion follows a circular path with the same period as the Moon takes to rotate around Earth. A similar effect is caused by the Sun but it is dominated by the perturbations due to the SRP which is presented in subsubsection 3.5.2.

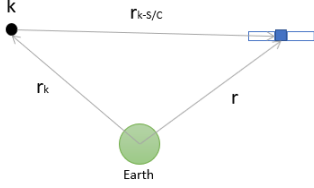


Figure 41: Orientation of the S/C and body k with respect to Earth.

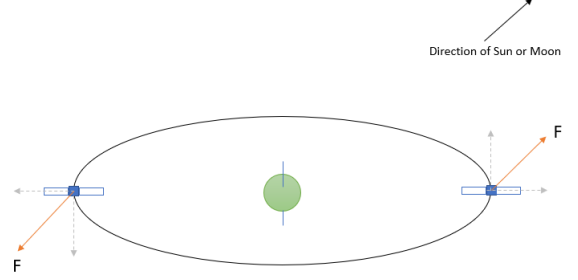


Figure 42: Net solar and lunar acceleration in Mean Equatorial Geocentric system.

D Longitude acceleration

Following Kepler's third law we recall that the relation between the mean motion n and the semi-major axis of a S/C is given by:

$$n = \frac{\sqrt{\mu}}{a^{\frac{3}{2}}} \quad (90)$$

Furthermore, the rate of change of the semi-major axis is presented by Lagrange as:

$$\frac{da}{dt} = \frac{2}{na} \frac{\partial R}{\partial \lambda} \quad (91)$$

A detailed derivation of the Lagrange planetary equation describing the variation of the oscillating orbital parameters is presented in [5]. Using Equation 90 and Equation 91, the longitude acceleration can be written as:

$$\frac{d^2 \lambda}{dt^2} = \frac{dn}{dt} = \frac{dn}{da} \frac{da}{dt} = -\frac{3}{a^2} \frac{\partial R}{\partial \lambda} \quad (92)$$

Recalling the model of the potential function presented in Equation 38 and the definition of the Legendre functions, Earth's gravitational potential up to $l = 3$ is given as:

$$\begin{aligned} R = \frac{\mu}{r} & \left\{ \frac{1}{2} J_2 \left(\frac{R_e}{r} \right)^2 + 3 J_{22} \left(\frac{R_e}{r} \right)^2 \cos [2 (\lambda - \lambda_{22})] \right. \\ & - \frac{3}{2} J_{31} \left(\frac{R_e}{r} \right)^3 \cos (\lambda - \lambda_{31}) + 15 J_{33} \left(\frac{R_e}{r} \right)^3 \cos [3 (\lambda - \lambda_{31})] \\ & \left. + \frac{3}{8} J_4 \left(\frac{R_e}{r} \right)^4 \right\} \end{aligned} \quad (93)$$

Finally, it follows from Equation 92 and Equation 93 that the longitudinal acceleration of a S/C is:

$$\begin{aligned} \ddot{\lambda} = -3n^2 & \left\{ -6 J_{22} \left(\frac{R_e}{r} \right)^2 \sin 2 (\lambda - \lambda_{22}) \right. \\ & + \frac{3}{2} J_{31} \left(\frac{R_e}{r} \right)^3 \sin (\lambda - \lambda_{31}) \\ & \left. - 45 J_{33} \left(\frac{R_e}{r} \right)^3 \sin 3 (\lambda - \lambda_{33}) \right\} \end{aligned} \quad (65)$$